HEAT AND FLUID FLOW IN MICROSCALE FROM MICRO AND NANO STRUCTURED SURFACES

TÜRKER İZCİ

Submitted to the Graduate School of Engineering and Natural Sciences
in partial fulfillment of
the requirements for the degree of
Master of Science

SABANCI UNIVERSITY

HEAT AND FLUID FLOW IN MICROSCALE FROM MICRO AND NANO STRUCTURED SURFACES

APPROVED BY:

Assoc. Prof. Dr. Ali Koşar .....

(Thesis Supervisor)

Prof. Dr. Erhan Budak .....

Assist. Prof. Dr. Güllü Kızıltaş Şendur .....

Assoc. Prof. Dr. Mehmet Yıldız .....

Assist. Prof. Dr. Çağlar Elbüken .....

DATE OF APPROVAL: 07/08/2012

HEAT AND FLUID FLOW IN MICROSCALE FROM MICRO AND NANO STRUCTURED SURFACES

Türker İzci

Mechatronics Engineering, M.Sc. Thesis, 2012

Thesis Supervisor: Assoc. Prof. Dr. Ali KOŞAR

Keywords: Micro pin-fin, heat sink, nanostructures, jet impingement, pool boiling, cooling application.

ABSTRACT

The use of enhanced surfaces became one of the most popular studies in order to increase heat transfer performances of microsystems. There are various techniques/processes applied to surfaces to enhance excess heat removal from microsystems. In parallel to these research efforts, various micro and nano structured surfaces were evaluated in channel flow, jet impingement and pool boiling applications.

In the first study, single micro pin-fins having the same chord thickness/diameter but different shapes are numerically modeled to assess their heat transfer and hydraulic performances for Reynolds number values changing between 20 and 140. The pin-fins are three dimensionally modeled based on a one-to-one scale and their heat transfer performances are evaluated using commercially available software COMSOL Multiphysics 3.5a. Navier-Stokes equations along with continuity and energy equations are solved under steady state conditions for weakly compressible and single-phase water flows. To increase the computational efficiency, half of the domain consisting of a micro pin-fin located inside a micro channel, is modeled using a symmetry plane. To validate the model, experimental data available in the literature are compared to simulation results obtained from the model of the same geometrical configuration as the experimental one. Accordingly, the numerical and experimental results show a good agreement. Furthermore, performance evaluation study is performed using 3D numerical models in the light of flow morphologies around micro pin-fins of various shapes. According to the results obtained from this study, the rectangular-shaped micro pin fin configuration has the highest Nusselt number and friction factor over the whole Reynolds number range. However, the cone-shaped micro pin-fin configuration has the best thermal performance index indicating that it could be more preferable to use micro pin fins of non conventional shapes in micro pin fin heat sinks.

In the second study, the results of a series of heat transfer experiments conducted on a compact electronics cooling device based on single and two phase jet impingement technique are reported. Deionized and degassed water is propelled into four microchannels of inner diameter $500\mu m$, which are used as nozzles and located at a nozzle to surface distance of 1.5mm. The generated jet impingement is targeted through these channels towards the surface of two nanostructured plates with different surface morphologies placed inside a liquid pool filled with deionized-water. The size of these nanostructured plates is 35mm x 30mm and they are composed of copper nanorods grown on top of a silicon wafer substrate of thickness $350\mu m$ coated with a 50 nm thick copper thin film layer (i.e. Cu-nanorod/Cu-film/Silicon-wafer). Nanorods were grown using the sputter glancing angle deposition (GLAD) technique. First type of nanostructured plates incorporates 600 nm long vertically aligned copper nanorod arrays grown with nanorod diameters and spacing varying between 50-100 and 20-100 nm, respectively. The second type incorporates 600 nm long tilted copper nanorod arrays grown with diameter values varying between 50-100nm and spacing in the range of 20-50 nm. Heat removal characteristics induced through jet impingement are investigated using the nanostructured plates and compared to the results obtained from a plain surface plate of copper thin film coated on silicon wafer surface. Heat generated by small scale electronic devices is simulated using four cylindrical aluminum cartridge heaters of 6.25 mm diameter and 31.75 mm length placed inside an aluminum base. Surface temperatures are recorded by a data acquisition system with four thermocouples integrated on the surface at various prescribed locations. Constant heat flux provided by the heaters is delivered to the nanostructured plate placed on top of the base. Volumetric flow rate and heat flux values are varied between 107.5-181.5 ml/min and 1-40 W/cm^2, respectively, in order to characterize the potential enhancement in heat transfer by nanostructured surfaces thoroughly. A single phase average heat transfer enhancement of 22.4% and a two phase average heat transfer enhancement of 85.3% has been realized using the nanostructured plate with vertical nanorods compared to flat plate. This enhancement is attributed to the increased heat transfer surface area and the single crystal property of the vertical Cu nanorods. On the other hand, nanostructured plate with tilted nanorods has shown poorer heat transfer performance compared to both the nanostructured plate with vertical nanorods and plain surface plate in the experiments performed. The lower heat transfer rate of the tilted Cu nanorods is believed to be due to the decreased supply of liquid jets to the base of the plate caused by their tilted orientation and closely spaced dense array structure. This leads to formation of air gaps that ultimately become trapped among the tilted nanorods, which results in reduced heat transfer surface area and increased resistance to heat transfer. In addition, non-single crystal structure of the tilted nanorods and resulting enhanced surface oxidation could further decrease their heat transfer performance.

In the third study, a nanostructure based compact pool boiler cooling system consisting of an aluminum base housing the heaters, a pool and four different plates to change the surface texture of the pool is designed. Effects of nanostructured plates of different surface morphologies on boiling heat transfer performance of the system are studied. Three nanostructured plates featuring Si nanowires of diameter 850 nm and of three different lengths, 900 nm, 1800 nm and 3200 nm respectively, which are etched through single crystal p-type silicon wafers using metal assisted chemical etching (MaCE), are utilized to enhance the pool boiling heat transfer. A plain surface Si plate is used as the control sample. Constant heat flux is provided to the liquid within the pool on the surface of the aluminum base through the plate by boiling heat transfer.

Existence of wall superheat gave rise to forming of vapor bubbles near the boiling temperature of the fluid, namely DI-Water. Bubbles emerged from the nanostructured plate along with the phase change. Nucleate boiling on the surface of the plate, bubble formation and bubble motion inside the pool created an effective heat removal mechanism from the heated surface to the liquid pool. Along with the enhancement in both boiling and single-phase region heat transfer coefficients, this study proves the ability of nanostructured plates in improving the performance of the cooling system.

MİKRO VE NANO YAPILI YÜZEYLERDEN MİKRO BOYUTTA ISI VE SIVI AKIŞI

Türker İzci

Mekatronik Mühendisliği, Yüksek Lisans Tezi, 2012

Tez Danışmanı: Doç. Dr. Ali KOŞAR

Anahtar Kelimeler: Mikro pin fin, ısı alıcı, nano yapılar, havuz kaynatma, jet akışı, soğutma uygulamaları.

ÖZET

Isı ve sıvı akış soğutma uygulamaları ısı transfer performanslarını arttırmak açısından mikrosistemlerin en popular çalışmalarından birisi haline gelmiştir. Sistemlerden ısıyı almak için çeşitli yöntemler kullanılmaktadır. Bu çalışmalara parallel olarak, mikro pin fin ısı alıcıları, jet soğutma ve havuz kaynatma yöntemleri ile çeşitli mikro ve nano yapılı yüzeyler değerlendirilerek en efektif yüzey araştırılmıştır. Örneğin mikro ısı alıcılarının, uzay endüstrisi, mikro reaktörler, elektronik soğutma, mikro türbin soğutma ve mikro biyoloji uygulamaları gibi çeşitli uygulama alanları vardır.

İlk çalışmada, mikro tek pin-finli mikro ısı alıcı modellenmiştir. Pin-finleri yükseklik çap oranları pin-fin'in yüksekliğini mikrokanalın yüksekliği ile aynı yükseklikte tutacak şekilde (250 μm) 0.5 ile 5 arasında değiştirilmiştir. Bu oranın 0.5 ile 5 arasında seçilmesi literatürde çok kullanılmasından ötürüdür. Bu çalışmada Reynolds sayısı aralığı da 20 ile 140 arasındandır. Reynolds sayılarının bu aralıkta seçilme sebebi ise literatürde düşük Reynolds sayılarındaki veri azlığıdır. Simülasyon yazılımı COMSOL Multi physics'in Weakly Compressible Navier-Stokes (Zayıf sıkıştırılabilir Navier Stokes) and Convection-Conduction (Taşınım, Iletim) modüleri gösterilen modele entegre edilmiştir. Bu yazılım Intel Xeon 3.0GHz processor ile işletilen 32GB RAM dahili belleğe sahip iş istasyonunda çalıştırılmıştır. Kullanılan işletim sistemi Microsoft XP 64bit Edition'dir. Hesaplama verimliliğini arttırmak için modelin sadece yarısı modellenip geri kalan yarısı simetri kenar olarak simulasyona dahil edilmiştir. Modelin sağlamasını yapmak için daha önce literatürde yapılmış deneysel çalışmanın simulasyonu yapılarak karşılaştırılmış ve sonuçlar birbiriyle örtüşmüştür. Elde edilen sonuçlara göre, dikdörtgen şeklindeki mikro pin fin dizilimi bütün Reynolds sayısı değerleri için en yüksek Nusselt sayısına ve sürtünme katsayısına sahip. Ancak, konik mikro pin fin dizilimi en iyi ısıl performans indeksi değerine sahip ve bundan dolayı

mikro pin fin ısı alıcılarında dairesel pin fin dizilimi gibi geleneksel mikro pin finler dışındaki şekilleri kullanmak tercih edilebilir.

İkinci çalışmada, tek ve çift fazlı lüle akış tekniğini temel alan ve kompakt bir elektronik devre soğutma cihazı üzerinde uygulanan nanoyapılar analiz edilmiştir. De-ionize su iç çapı 584 μm olan ve ağız-yüzey mesafesi 1.5mm olarak ayarlanan dört mikrokanala gönderilmiştir. Oluşturulan su jetleri bu kanallar vasıtasıyla farklı yüzey morfolojilerine sahip ve deionize su ile doldurulmuş tankın içine yerleştirilmiş iki farklı nanoyapılı levhanın yüzeylerine püskürtülmüştür. Nanoyapılı levhaların boyutları 35mmx30mm olup 350 μm kalınlığındaki ve 50 nm kalınlığında ince bakır film ile kaplanmış silikon yonga üzerinde oluşturulmuş bakır nanoçubuklardan meydana gelmişlerdir. Nanoçubuklar sputter glancing angle deposition (GLAD) ekme tekniği kullanılarak büyütülmüştür. Birinci tip nanoyapılı levha yaklaşık 600 nm boyunda ve yüzeye dik olarak uzanan, çapları 50-100 nm ve aralıkları 20-100 nm arasında değişen nanoçubuklar barındırmaktadır. İkinci tip ise 600 nm uzunluğunda ve yüzeyden eğimli olarak çıkan nanoçubuklardan oluşurken, bu nanoçubukların çapları 50-100 nm arasında değişmekte ve çubukların birbirine uzaklığı 20-50 nm arasında değişmektedir. Sistemin lüle jet akışı tesirindeki ısı uzaklaştırma performansı nanoyapılı levhalar kullanılarak test edilmiş ve elde edilen sonuçlar nanoyapılı levha yerine silikon yonga üzerine kaplanmış düz bakır yüzeyli levha kullanılarak elde edilen verilerle karşılaştırılmıştır. Nanoyapılı yüzeylerin ısı transferine katkılarını daha iyi analiz etmek amacıyla hacimsel debi ve ısı akısı için göreceli olarak tek fazda 107.5-181.5 ml/dk ile 10000-57143 W/m^2, çift fazda ise 107.5-144.5-181.5 ml/dk ile 10000-400000 W/m^2 arasında değişen değerlerde deney gerçekleştirilmiştir.

Üçüncü çalışmada, nano-yapılı yüzeyleri temel alan, ısıtıcıların içinde bulunduğu alüminyum bir taban, bir havuz ve havuzun yüzey morfolojisinin değiştirilmesine yarayan dört farklı levhadan oluşan kompakt bir havuz kaynaması soğutucu sistemi tasarlanmıştır. Farklı yüzey yapısına sahip nano-yapılı levhaların sistemin kaynama ısı transferi karakteristiklerine etkisi incelenmiştir. 850 nm çapında ve sırasıyla 900 nm, 1800 nm ve 3200 nm uzunluğunda nano-çubuklara sahip üç farklı nano-yapılı levha, havuz kaynaması ısı transferini artırmada kullanılmıştır. Düz yüzeyli silikon levha ile kontrol deneyi yapılmıştır. Havuz içerisindeki sıvıya, altında bulunan alüminyum taban vasıtasıyla sabit ısı akısı kaynama ısı transferi ile aktarılmıştır. Wall superheat, sıvının, yani distile suyun kaynama noktasına yaklaşıldığında buhar baloncuklarının oluşmasını sağlamıştır. Faz değişimi ile birlikte nano-yapılı levhadan baloncuk çıkışı gözlenmiştir. Levha yüzeyindeki nucleate boiling ile havuz içerisinde baloncuk oluşumu ve baloncuk hareketi ile ısıtılan yüzeyden sıvıya verimli bir şekilde ısı aktarımı sağlanmıştır. Düz silikon levha kullanıldığında, kaynama başlangıç noktasında yüzey sıcaklığı 104 ºC olarak ölçülürken, nano-yapılı levha kullanımıyla bunun 100 ºC yakınlarına düştüğü görülmüştür. Kaynama ısı transferi katsayılarında meydana gelen iyileşmenin yanı sıra, bu çalışma nano-yapılı levhaların sistemin ısı transfer performansına olumlu etkisini de kanıtlamıştır.

ACKNOWLEDGEMENTS

I wish to express my sense of gratitude to Dr. Ali KOŞAR for his boundless guidance and advices during my study, and for the fruitful long discussions we had together with him even during his intensive working hours. I am very lucky to have worked with him.

I would also like to thank our collaborators that have rendered this work possible: Dr. Tansel Karabacak and Wisam Khudhayer from University of Arkansas at Little Rock.
I am also grateful to my thesis committee members Dr. Erhan Budak, Dr. Güllü Kızıltaş Şendur, Dr. Mehmet Yıldız and Dr. Çağlar Elbüken for giving their valuable time commenting on my thesis and their valuable ideas during my study in this university.

I would like to express my thanks to my colleagues and friends Alihan Kaya and Talha Boz, and lab officers for their superior support and friendship.

I'd like to acknowledge the financial support Tubitak BIDEB provided me with during my graduate studies and hereby present my gratitude.

Finally, I would like to thank to my family, Osman Yavuz Perk and Ebru Demir for their love and endless patience they've shown. I would like to thank them for being there for me everytime I needed and not withholding their precious support.

TABLE OF CONTENTS

LIST OF FIGURES

LIST OF TABLES

NOMENCLATURE

2D	Two Dimensional
3D	Three Dimensional
A	Area, m^2
BND	Boundary
C	Heat Capacity, J/kg.K
D	Fin Diameter, m
DOF	Mesh degrees of freedom
f	Friction factor
h	Heat transfer coefficient, $W/(m^2.K)$
H	Fin and micro channel height, m
k	Conductivity, W/(m.K)
L	Length, m
MES	Maximum mesh element size
$\mathbf{n}$	Normal vector to a surface
Nu	Nusselt number
P	Pressure, Pa
P	Power input to the system, W
q	Heat flux, W/m^2
$\mathbf{q}$	Heat flux vector
r	Radius of pin-fin, m
R	Thermal resistance, K/W
Re	Reynolds number
SBD	Sub domain
T	Temperature, K
$\mathbf{u}$	Velocity vector of the fluid, m/s
u, v, w	Velocity components of the fluid, m/s
W	Width of the fluid domain, m
$\boldsymbol{x}$	Spatial coordinate vector
x, y, z	Spatial coordinates

Greek Letters

η	Thermal Performance Index TPI, Dimensionless
μ	Dynamic viscosity, Pa.s
ρ	Mass density, kg/m^3

Subscript

amb	Ambient
c	Cross sectional
cir_base	Circular pin fin as a reference base
cond	Conductive
conv	Convective
fin	Fin
hb	Heated base
hs	Heated surfaces
heat	Heated fluid
i	Initial
in	Inlet
max	Maximum

out	Outlet
sur or *s*	Surface
sat	Saturation
tot	Total

1 INTRODUCTION

1.1 The Effect of Micro Pin-Fin Shape on Thermal and Hydraulic Performance of Micro Pin-Fin Heat Sinks

1.1.1 Overview on Heat Sink

A heat sink is a passive cooling component that cools by dissipating heat into the surrounding area. Light weight solutions of thermal management is crucial for densely packed and high heat flux dissipating microelectronic devices used in aerospace and other demanding industries [1, 2]. A heat sink is designed to increase surface area in contact with the coolant such as air or water, to obtain a higher contact area of heated surface with the surrounding area. Heat sinks are generally used to cool CPUs and graphic porccesors of computers as shown in Figure 1.1.

Figure 1.1. CPU cooling with a heat sink and a fan **[3]**.

Such as, a computer's CPU works at a rapid pace during the intensive calculations and then it starts to generate more heat. This temperature increase should be kept in check in order to prevent processor overheat and damage. Fortunately,

today's new genearation processors include a heat sink, which dissipates heat from the heat sink preventing from overheat. A fan and a heat sink are both used as a cooler for CPUs. The use of fluid coolants instead of air is a must for heat removal from energy sources with high heat fluxes. Plain micro channels have been modified to more complex structures with micro pin-fins, which were integrated into them by the help of recent advancements in micro fabrication techniques [2, 4, 5, 6, 7, 8, 9, 10, 11, 12].

1.1.2 Literature Survey on Micro Pin Fin Heat Sink Study

Micro pin-fin heat sinks consist of a micro channel with an array of either staggered or in line micro pin-fins so that they typically have the same height (*H*) as the micro channel. Moreover, these devices are mostly operated with water as the working fluid. The Reynolds number (*Re*) of the flow across the pin-fins usually does not exceed 1000. Previous studies analyzed pin-fin heat sinks of various pin-fin shapes such as circular [13, 14, 15, 16, 17, 18, 19, 20, 21], cone shaped [17], diamond shaped [14, 20, 21, 22], hydrofoil shaped [17, 23], square [8, 9, 10, 11, 20, 21], triangle [20, 21] and rectangular [2, 5, 19] pin-fins. While some of the studies were conducted on pin-fins of sizes on the order of millimeters [1, 2, 9], the rest dealt with pin-fins of sizes on the order of micrometers [4, 6, 7, 8, 10, 11, 12, 17, 20, 21].

The literature currently covers micro pin fin heat sinks' hydrodynamic and thermal characteristics and gives valuable information about this subject [13, 14, 15, 16, 17, 18, 19, 20, 21, 24] [25, 26, 27, 28, 29]. The study of Peles et al. [13] emphasized that very low thermal resistances could be achieved by using micro pin fin heat sinks. The macro scale studies of Jeng and Tzeng [30] and Kahn et al. [31] compared the performances of various macro scale pin fin geometries such as rectangle, square, circle and ellipse shapes. Jeng and Tzeng [30] observed that the circular pin fins had more pressure drop than the square pin-fins at high Reynolds number *Re* and also had higher heat transfer performance than the square pin fins. The study of Kahn et al. [31] concluded that square pin fins have the worst performance in terms of heat transfer, drag force and total entropy generation, where circular pin fins have the best performance for low *Re*, small dimensions and high aspect ratios. None of the studies cover a certain pin-fin shape rather than a collection of micro pin-fin shapes except the studies of Koşar and Peles [17] and Tullius et al. [20, 21]. Koşar and Peles [17] compared the hydrodynamic and thermal performances of micro pin-fin heat sinks

having circular, rectangular, hydrofoil and cone shaped micro pin-fins. The study concluded that the denser pin fin configuration has better performance at high *Re* values, the less dense pin fin configuration is better at low *Re* values. The best thermal performance at low Re values (Re<40) is observed while using rectangular pin fin configuration, and even though 2CD (circular) pin fins have the best results at moderate Re values (40<Re<100), the best performance at high Re values (Re>100) is obtained by replacing them with 4C (cone shaped) pin fins. Furthermore, 2CLD (circular less dense) pin fins has the best hydrodynamic performance at low Re values (Re < 50), whereas hydrofoil pin fins turned out to be the best choice for Re values above 50. Tullius et al. [20, 21] compared the thermal performances of micro pin-fin heat sinks having circle, square, triangle, ellipse, diamond and hexagon shaped micro pin-fins in a staggered array, which are attached to the bottom heated surface of a rectangular minichannel. Effects of fin height, width, spacing and changing material are investigated, and the best performance is observed with triangular pin fins with larger fin height, smaller fin width, and the spacing as much as double the fin width by maximizing the number of fins in each row. John et al. [19] investigated the effect of pin fin geometry for square and circular micro pin fins. They observed that the circular pin-fins had better performance compared to the square pin-fins at *Re* values below 300, while the square pin fins had better performance compared to the circular pin fins at higher Re values. Koşar et al. [32] investigated pressure drop in 3 different micro pin-fin heat sinks under unstable boiling conditions. They found that the magnitude of the pressure drop fluctuations was not significant regardless of the shape of the pin fin. Liu et al. [33] studied the flow and heat transfer performance of the square long pin fins for Reynolds numbers between 60 and 800. They concluded that pressure drop and Nusselt number increased with the increasing Reynolds number. Their type 1 heat sink, which has larger square pin fin perimeter than type 2, has larger thermal resistances for small pressure drop (lower than 1.1 kPa) but smaller thermal resistances for larger pressure drops than type 2 heat sink.

Most of the previous studies utilize experimental data to compare them to the existing conventional correlations for predicting Nusselt numbers or friction factors of micro pin-fin heat sinks. There are only few numerical studies for accurately simulating heat and fluid flow and discussing flow morphologies in micro pin-fin heat sinks [6, 7, 8, 9]. Moreover, there are also very few parametric numerical studies focusing on the effect of micro pin-fin shape on heat transfer performance. This research aims at

enhancing understanding about this subject by showing thermal and hydraulic characteristics of a single micro pin-fin having various shapes (circular, cone shaped, diamond, hydrofoil shaped, square, rectangular, and triangular). Microfabrication technology enables the formation of unconventional pin fin geometries so that an enhancement in thermal-hydraulic performance with changing the micro pin fin geometry could be viable. For this purpose, water flow in the micro channel is simulated for Reynolds number between 20 and 140 in similar lines to Koz et al. [34], and streamlines around the modeled micro pin fins are obtained and utilized to enrich the discussion about the performances obtained from different micro pin fin configurations.

The novelty of this work lies in the fact that by zooming-in on a single pin fin along the channel it is possible to filter out the effect of changing pin fin shape on the performance of the heat sink. Thus, a much clearer understanding of the physics behind the cross-flow over finned surfaces is obtained. For this purpose, single micro pin fin configurations are simulated for providing better and precise analysis, and a possible multi pin fin configuration for this study could be considered as repetitions of single micro pin fin configurations along the heat sink. Heat transfer coefficients, Nusselt numbers, friction factors and thermal performance indices are obtained for each configuration with a single micro pin fin to discuss about the effect of the micro pin fin shape, and a comprehensive performance evaluation is performed to show the effect of the micro pin fin shape on the thermal-hydraulic performance.

1.2 Submerged Jet Impingement Cooling using Nanostructured Plates

1.2.1 Literature Survey on Jet Impingement Cooling

In terms of the capability of providing high heat transfer rates, jet impingement is one of the most efficient cooling mechanisms. Jet impingement cooling not only offers high heat transfer rates but also has the benefit of removing all thermal interface resistances between the surface and the cooling fluid [35]. In a wide range of industrial applications such as annealing of metals [36], cooling of gas turbine blades [37], cooling in grinding processes [38], and cooling of photovoltaic cells [39] jet impingement cooling became a preferential method for the heat transfer community. For instance, in gas turbine applications, this cooling method has been used for a long

time in order to assure durability during long operating intervals [36]. Moreover, impingement systems play an important role in micro scale applications such as cooling of electronic components, microprocessors, and MEMS devices [35].

Recently, microstructured [40] and nanostructured surfaces [41], [42], [43] have been utilized to achieve high heat transfer performance due to their enhanced heat transfer area and positive effect on heat transfer coefficients with diminishing length scales. In order to keep up with the miniaturization process, heat transfer and fluid flow at micro and nano scales have been rigorously studied in the literature to achieve higher heat removal capabilities [44], [45], [46].

Flow and heat transfer characteristics of multiple impinging jets can differ substantially from those of single jets depending mainly on geometrical conditions. If there are more jets in the array and the individual jet diameter is smaller, the heat transfer rates will be higher [35]. Multiple jet flows interact with each other so that employing jet arrays becomes considerably complex or even erroneous compared to single jet configurations. While heat transfer rates for single jets can be functionally expressed by relatively simple power-functions of Reynolds (Re) and Prandtl (Pr) numbers, correlations for heat transfer rates for multiple jets require the consideration of a number of additional characteristic numbers such as nozzle to surface distance and nozzle spacing [47]. Heat transfer in jet impingement systems is greatly influenced by nozzle geometry. In previous studies reported in the literature, for a constant Reynolds number, it was found that decreasing the jet diameter yields higher stagnation and average heat transfer coefficients [48], [49], [50]. This can be attributed to the higher jet velocities created by the smaller nozzles [36].

The aim of this study is to extend the ongoing research on jet impingement to nanostructured surfaces. For this purpose, the thermal properties of two types of nanostructured plates based on vertical and tilted copper nanorods fabricated by glancing angle deposition (GLAD) technique [51], [52], [53] were investigated and their effect on the performance of heat removal is compared to that obtained using a plain plate coated with flat Cu thin film. In addition, multiple impinging jets were used instead of a single jet where heat transfer under an impinging jet is very high in the stagnation zone but decreases quickly away from the jet [35]. Employed multiple jet arrays increase the number of available stagnation zones, and thus, they enhance the heat transfer from the impingement surface. This study reveals the advantages of using nanostructured surfaces and multiple impinging jets in microscale cooling. Moreover,

there is little information and studies concerning the heat transfer performance of the nanostructured surfaces with tilted nanorods. It has been reported that nanostructures enhance the heat transfer performance in boiling applications by decreasing the contact angle of the liquid and therefore enhancing wettability [54]. However, there is a lack of knowledge concerning their performances and their configuration effects in jet impingement cooling systems. This study is also meant to display the effect of the orientation of nanostructures (tilted and vertical nanorods) on heat transfer during jet impingement.

1.3 A Compact Pool Boiler Utilizing Nanostructured Plates for Microscale Cooling Applications

1.3.1 Motivation

Along with the miniaturization of individual components constructing electronic devices, functionality of such devices increased greatly due to the ability of tightly packaging these components. Recent developments in technology made it possible for electronic devices to have day to day increasing computational powers while diminishing in size. While benefitting from miniaturization process in increasing the mobility, heat dissipated per unit area by such devices increased greatly, therefore the development of more effective and equally miniaturized cooling systems became a priority in order to preserve the functionality and stability of such devices. Conventional methods such as using air and fan systems and even their improved versions with fin arrays started to fail as the heat removal problems became more demanding. Due to the superior heat removal characteristics of different liquids, a paradigm shift in cooling applications became inevitable, so using liquids as coolants became a popular trend. Most of the experiments featuring different liquids presented promising results [55]. Still, some advanced electronic systems demanding removal of very high heat fluxes rendered single phase liquid cooling applications insufficient [56]. In order to achieve higher efficiency in miniaturized cooling systems, focus of this particular research area has shifted towards cooling applications benefitting from phase-change, such as jet-impingement, flow boiling in micro-channels and pool boiling. Experiments have repeatedly shown that two-phase cooling systems yield better results than single-phase applications [55].

1.3.2 Literature Survey on Pool Boiling

Though the boiling applications are not limited with pool boiling, it is one of the most popular heat removal mechanisms and is being studied by many researchers. Another hot topic is the effect of nanoparticles and nanostructured surfaces on heat transfer characteristics of cooling systems. So, it became a rising trend in heat transfer community to couple these methods that are known to be effective in heat removal [57, 43, 58]. Many experiments have proven that nanofluids [59, 60, 61, 62, 63, 64] and nanostructured surfaces [54, 65, 66, 67, 68] are very compatible with pool boiling applications and make a significant enhancement in heat removal performance of such systems. It has been shown that the heat transfer coefficients and CHF increase greatly when nanostructured plates and nanofluids are utilized in pool boiling applications, furthermore, dramatic reductions in boiling inception temperatures have been reported [59, 60, 61, 69, 62, 63, 64, 54, 65, 66], [67]. Capability of such surfaces in decreasing the contact angle and increasing wettability in boiling applications has been reported in literature [70, 64, 69, 71, 66].

The novelty of this study is that it aims to contribute this popular research topic by investigating the effect of varying nanowire length on heat removal performance of pool boiler cooling systems. Three nanostructured plates, each featuring Si nanowires of different lengths and of same diameter have been experimented on and the results are compared to the measurements made using a plain surface Si plate. Surface temperatures are recorded for each of the plates in various heat fluxes starting from single-phase region and promising results are obtained as presented in this paper.

2 METHODOLOGY AND PROCEDURE

2.1 Methodology and Procedure for Micro Pin Fin Heat Sink Study

2.1.1 Drawing

The numerical models do not have the exactly same geometry as a typical micro heat sink with an array of many pin-fins inside. Instead, without simulating the pin-fin interactions, only a single pin-fin is drawn in a micro channel. A sample of 2D and 3D representations of the micro heat sink geometry with a circular micro pin-fin and a symmetry plane is depicted in Figure 2.1 and Figure 2.2. Figure 2.1 shows the cross section of the circular pin-fin heat sink with symmetry plane, appropriate dimensions, and relative position of the micro pin-fin with respect to the micro channel. Figure 2.2 shows the 3D view of the circular pin-fin heat sink with its symmetry plane, three sub domains, and heated pin-fin base, while Figure 2.3 shows the cross sections of the pin-fins used in this study.

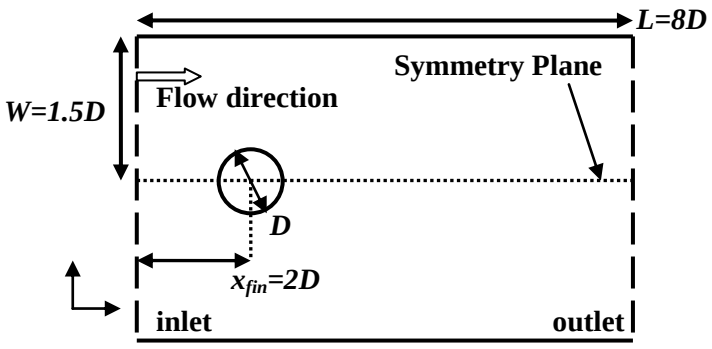

Figure 2.1. Cross section of a typical micro heat sink model with a circular micro pin-fin.

All micro pin-fins in this work have a chord thickness or diameter (D) of 100 μm, while the height of the micro channel and pin-fins (H) are set to 250 μm. The length of the cone shaped fins (L_{fin}) is 290 μm, while the length of the hydrofoil shaped chord length and rectangular pin fins are 500 μm. The dimensions were selected according to the dimensions of micro pin fin configurations in the literature [34].

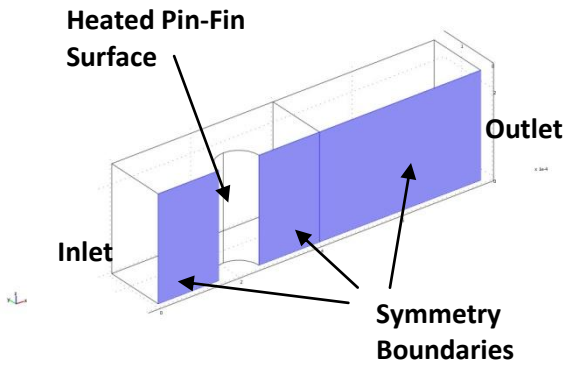

Figure 2.2. Important components a typical micro heat sink model with a circular fin in 3D representation.

Half of the domain is simulated by using the symmetry plane, and the upper half domain in Figure 2.1 always consists of a half micro pin fin. The half width of the micro channel, *W*, is kept as 1.5 times greater than the chord thickness or diameter, *D*. The fin-center-to-channel-wall distance of *1.5D* is chosen as the same as the minimum fin-to-fin distance available in the literature. Moreover, the channel length, *L*, is set equal to *8D* in accordance with [34]. Finally, the pin fins are positioned on the symmetry plane with a distance of $x_{fin}=2D$ from the inlet.

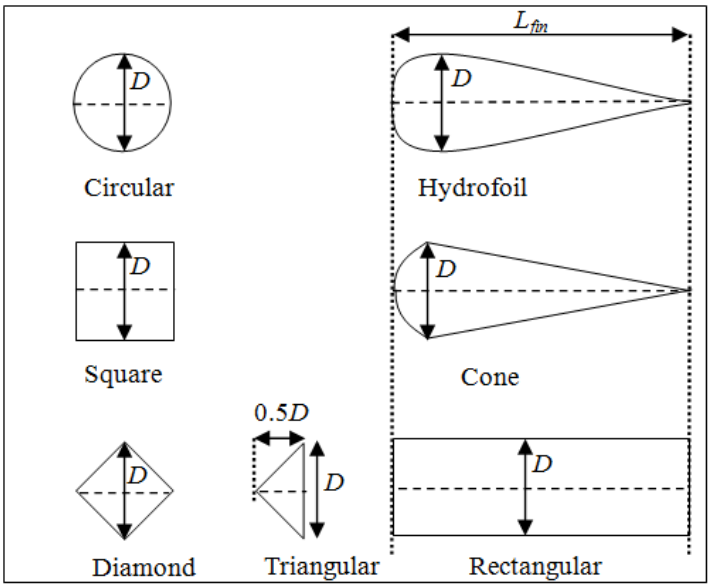

Figure 2.3. Cross sections of micro pin-fins used in the current study.

2.1.2 Fluid Flow

Due to the varying temperature profile of water throughout the micro channel, flows in all the models are governed by weakly compressible, stationary Navier-Stokes equations. Therefore, the physical properties of water such as mass density (ρ) and dynamic viscosity (μ) are all subjected to change because of the varying temperature. Navier-Stokes equations are represented in a fully compressible formulation with the continuity equation:

$$\nabla.(\rho\mathbf{u}) = 0 \tag{1}$$

$$\rho\mathbf{u}.\nabla\mathbf{u} = -\nabla p + \nabla.\left(\mu(\nabla\mathbf{u} + (\nabla\mathbf{u})^T) - \frac{2}{3}\mu(\nabla\mathbf{u})\mathbf{I}\right) \tag{2}$$

The boundary condition at the inlet is a variable inlet velocity (u_{in}):

$$\mathrm{u.n}|_{\mathrm{x=0,y,z}} = \mathrm{u_{in}} \tag{3}$$

Local Reynolds number across the fin is defined according to the equations below:

$$Re = \frac{\rho D u_{max}}{\mu} \tag{4}$$

$$u_{max} = \frac{W}{W-r}u_{in} = \frac{1.5D}{1.5D-0.5D}u_{in} = \frac{3}{2}u_{in} \tag{5}$$

Where r is the radius of the pin-fin.

The Reynolds numbers to be simulated are 20, 30, 40, 50, 60, 80, 100, 120 and 140. u_{in} is calculated using the following expression:

$$\mathrm{u_{in}} = \frac{2}{3}\frac{\mathrm{Re}\mu}{\mathrm{D}\rho\mathrm{W}} \tag{6}$$

The outlet is set as an open boundary with no normal stress:

$$[-P\mathbf{I}].\mathbf{n}|_{x=L,y,z} = 0 \quad (7)$$

Symmetry boundary condition is imposed for one side of the channel as shown in Figure 2.4. The symmetry plane cuts the micro channel, and the fin is located in the middle of channel width. All other boundaries are set as non-slip boundary conditions.

2.1.3 Heat Transfer

For all the models, steady state conditions are imposed for convection and conduction. All the properties of water such as mass density (ρ), heat capacity (C) and conductivity (k) are taken as temperature dependent. Water is assumed to stay in liquid form, and viscous heating is neglected.

The governing energy equation is expressed as:

$$\rho C\left(\mathbf{u}\cdot\nabla\right)T = -\left(\nabla\cdot q\right) = \nabla\cdot\left(k\nabla T\right) \quad (8)$$

The heat flux (q_{in}) is applied on the micro pin-fin surface as the values presented in Table 2.1.

$$\mathbf{q}.\mathbf{n}|_{fin,surface} = q_{in} \quad (9)$$

Applied heat flux values are chosen in such a way that outlet temperatures vary from 330 to 370 K in the Reynolds number range of this study.

Table 2.1. Applied heat fluxes to pin-fin bases, q_{in} versus fin shape.

Fin Shape	q_{in} (W/m^2)
Circular	3x10^6
Cone	3x10^6
Diamond	3x10^6
Hydrofoil	2x10^6
Rectangular	2x10^6
Square	3x10^6
Triangular	3x10^6

Additionally, the inlet temperature (T_{in}) is constant and set to 300 K:

$$T|_{x=0,y,z} = T_{in} \tag{10}$$

The channel outlet is adjusted to have outward convective flux:

$$\mathbf{q}.\mathbf{n}|_{x=L,y,z} = \rho C T \mathbf{u}.\mathbf{n}|_{x=L,y,z} \tag{11}$$

All the other boundaries are set as thermally insulated.

2.1.4 Mesh and Solver Settings

The simulation package, COMSOL Multi physics 3.5a, is used and its Weakly Compressible Navier-Stokes and Convection-Conduction modules are integrated to the model presented above. This software is synchronized with Solid Works 2008 SP2.1 to perform geometric sweeps. This software runs in a work station with an Intel Xeon 2.67 GHz processor with 24GB RAM. The server's operating system is Microsoft XP 64bit edition.

As presented in Figure 2.3, cone shaped, hydrofoil shaped, and rectangular cross sections have both short and long edges. The long edges do not face the flow as directly as short edges. Therefore, the fluid flow resolution needs to be lower, and they are to be meshed with larger boundary elements when compared to short edges. The maximum element sizes (MES) for boundaries, sub domains, and their corresponding degrees of freedom (DOF) are presented in Table 2.2.

Table 2.2. Maximum mesh element sizes and numbers of degrees of freedom.

	BND 1 MES (μm)	BND 2 MES (μm)	SBD MES (μm)	# DOF
Circular	3	3	15	1327697
Cone	5	10	15	993885
Diamond	5	5	18	790473
Hydrofoil	5	10	15	1169166
Rectangular	5	10	15	882522
Square	5	5	25	686675
Triangular	4	4	15	1087952
Circular(Grid Dependency Test)	3	3	11	2247712

Mesh elements on the surfaces and volumes are triangular and tetrahedral, respectively. Total number of degrees of freedom can vary from 686675 to 1327697. As a result, a single simulation can take from 2 to 3 hours. There are 7 geometries with 8 Reynolds numbers. The total time required for all simulations to be completed is approximately 2.5 x 7 x 8 = 140 hours. The trials with 2 different mesh densities (very high and intensive) yielded differences less than 5%, which were assumed as negligible. Thus, lower density mesh has been used in analytical solving procedures due to its better time and CPU consumption efficiency. A sample of a mesh configuration of selected mesh density is displayed in Figure 2.4.

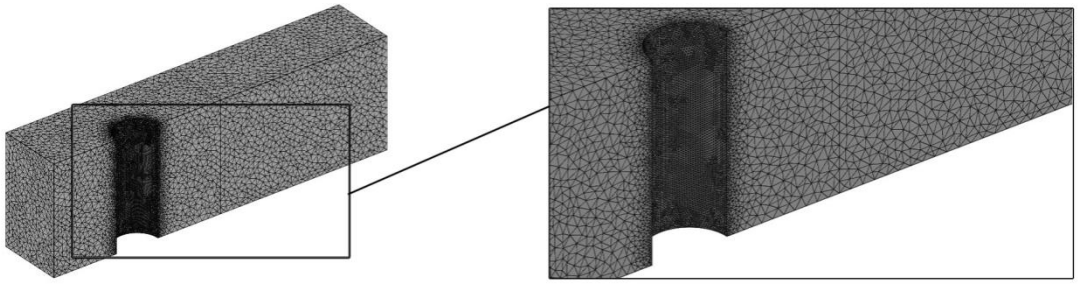

Figure 2.4. Mesh configuration of the circular shaped pin fin heat sink.

To solve the governing equations, segregated parametric solvers are used for two variables sets, which are fluid flow (u, v, w and P) and heat transfer (T) modules. Biconjugate gradient stabilized iterative method solver (BICGStab) [72, 73] is used for both modules with a tolerance and factor in error estimate of 10^{-3} and 20, respectively. As the preconditioner of BICGStab solver, Geometric Multigrid solver is used with Vanka pre and post smoothers and PARDISO (Parallel Sparse Direct Linear Solver) coarse solver.

2.1.5 Post Processing of the Results

For the validation model, the pressure difference between the inlet and the outlet is given, and the resulting flow velocity is compared to the experimental results of [17].

In order to accurately evaluate the pressure loss that micro pin-fins introduce, total force in the x direction (F_x) is integrated over pin-fin surfaces, then surface averaged and substituted for channel pressure difference:

$$\Delta P = \frac{\int_{\text{Fin surfaces}} F_x dA}{A_{fin,sur}} \tag{12}$$

Friction factor for each pin-fin is expressed as:

$$f_{fin} = \frac{2(\Delta P_{fin})}{\rho u_{max}^2} \tag{13}$$

In order to evaluate the heat transfer performance of the models, the outlet, ambient, pin-fin and heated base temperatures need to be calculated by using the following equations, respectively:

$$T_{out} = \frac{\int_{\substack{\text{outlet} \\ \text{surface}}} TdA}{A_{out}} \tag{14}$$

$$T_{amb} = \frac{T_{in} + T_{out}}{2} \tag{15}$$

$$T_{fin} = \frac{\int_{A_{fin,sur}} T.dA}{A_{fin,sur}} \tag{16}$$

By using the following equations, average heat transfer coefficients (h) and Nusselt number (Nu) are calculated in similar lines to previous experimental studies in the literature [15, 17, 23]:

$$Nu = \frac{hD}{k} \tag{17}$$

$$h = \frac{q_{in}}{[T_{fin} - T_{amb}]} \tag{18}$$

Thermal-hydraulic performance is assessed in terms of thermal performance index (TPI), η, which is the heat transfer enhancement to the pumping power ratio [74,

75]. Circular micro pin fin values are taken as the reference for the comparison to the other pin fin geometries:

$$\eta = \frac{Nu/Nu_{cir,base}}{(f/f_{cir,base})^{1/3}} \quad (19)$$

2.2 Experimental Setup and Procedure of Jet Impingement Study

2.2.1 Overview on Nanostructured Plates

GLAD technique is a self-assembly growth technique that can provide a novel capability for growing 3D nanostructure arrays with interesting material properties such as high electrical/thermal conductivity and also reduced oxidation compared to the polycrystalline films [51], [52], [53]. It offers a simple, single-step, cost- and time-efficient method to fabricate nanostructured arrays of various elemental materials as well as alloys and oxides. The GLAD technique uses the shadowing effect which is a physical self-assembly process, through which some of the obliquely incident atoms may not reach certain points on the substrate due to the concurrent growth of parallel structures. Due to the statistical fluctuations in the growth and effect of initial substrate surface roughness, some rods grow faster in the vertical direction. These longer nanorods capture the incident atoms, while the shorter rods get shadowed and cannot grow anymore. This leads to the formation of isolated nanostructures. In addition, nanostructures with different shapes such as vertical tilted, helical, or zigzag geometries can be obtained by introducing a substrate rotation around the surface normal axis. The shadowing effect, and therefore shapes and sizes of nanostructured arrays of GLAD, can be controlled by adjusting the deposition rate, incidence angle, substrate rotation speed, working gas pressure, substrate temperature, and the initial surface topography of the substrate.

2.2.2 Nanostructure Deposition

The schematic of the custom-made GLAD experimental setup in the present study is shown in Figure 2.5. For the fabrication of vertically aligned and tilted Cu nanorod arrays, the DC magnetron sputter GLAD technique is employed. Cu nanorods were deposited on the native oxide p-Si (100) substrates ($2cm^2$) coated with a 50 nm

thick flat Cu film using a 99.9% pure Cu cathode (diameter about 7.6 cm). The substrates were mounted on the sample holder located at a distance of about 12 cm from the cathode.

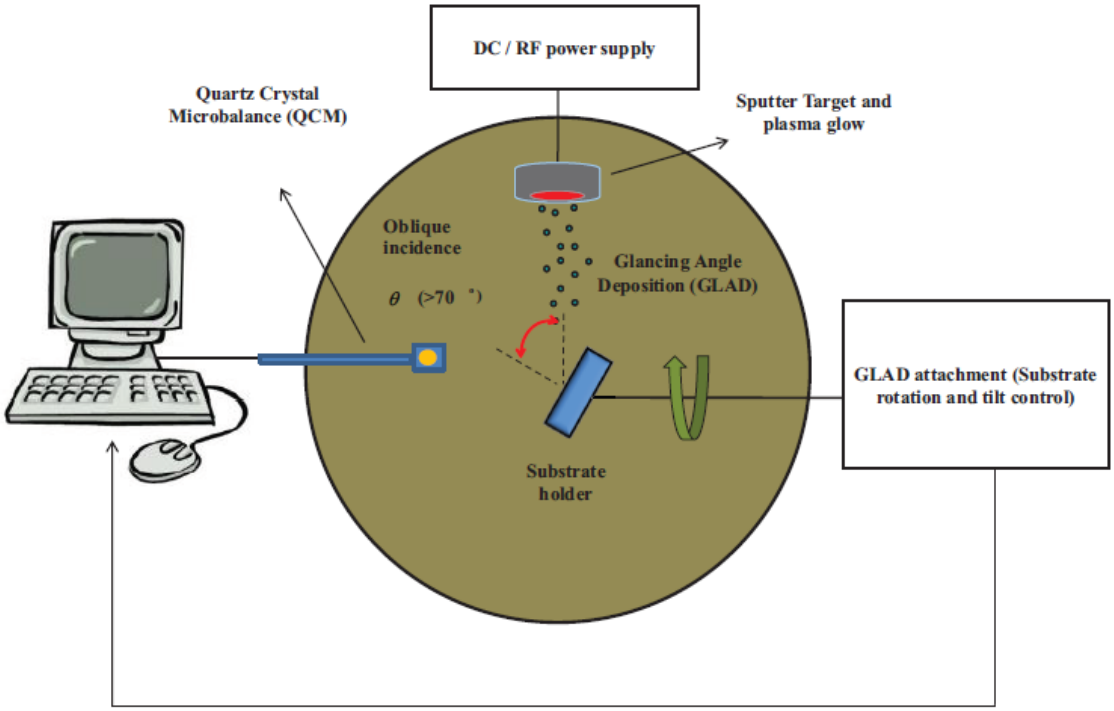

Figure 2.5. A schematic of the glancing angle deposition (GLAD) technique used for the fabrication of vertical and tilted copper nanorod arrays.

For GLAD growth, the substrate was tilted so that the angle θ, between the surface normal of the target and the surface normal of the substrate is 87 °. The substrate was attached to a stepper motor and rotated at a speed of 2 rpm for growing vertical nanorods, while the substrate was not rotated for the deposition of tilted nanorods. The depositions were performed under a base pressure of $6.5x10^{-7}$ Torr, which was achieved by utilizing a turbo-molecular pump backed by a mechanical pump. During Cu deposition experiments, the power was 200 W with an ultrapure Ar working gas pressure of 2.5 mTorr. The deposition time of GLAD Cu nanorods was 60 min. For comparison purposes, conventional smooth Cu thin film samples (i.e. plain surface configuration) were also prepared by normal incidence deposition (θ = 0 °) with a substrate rotation of 2 rpm. Deposition rate of the vertical nanorods was measured utilizing quartz crystal microbalance (Inficon - Q-pod QCM monitor, crystal: 6 MHz gold coated standard quartz) measurements and cross-sectional scanning electron microscopy (SEM) image analysis to be about 8.6 nm/min. The SEM unit (FESEM-6330F, JEOL Ltd, Tokyo, Japan) was used to study the morphology of the deposited

nanorods. The top and side view SEM images of vertical Cu nanorods are shown in Figure 2.6(b) in which an isolated columnar morphology can be seen. However, for the conventional Cu film deposited at normal incidence, its surface was observed to be flat as indicated by the SEM image (Figure 2.6(a)). As can be seen from Figure 2.6(b), the top of the vertical nanorods has a pyramidal shape with four facets, which indicates that an individual nanorod has a single crystal structure. This observation was confirmed by previous studies [76], [77], [78] and Khudhayer et al.'s recent work [79] which reported that individual metallic nanorods fabricated by GLAD are typically single crystal. Single crystal rods do not have any interior grain boundaries and have faceted sharp tips. This property will allow reduced surface oxidation, which can greatly increase the thermal conductivity, robustness, and resistance to oxidation-degradation of our nanorods in the present study.

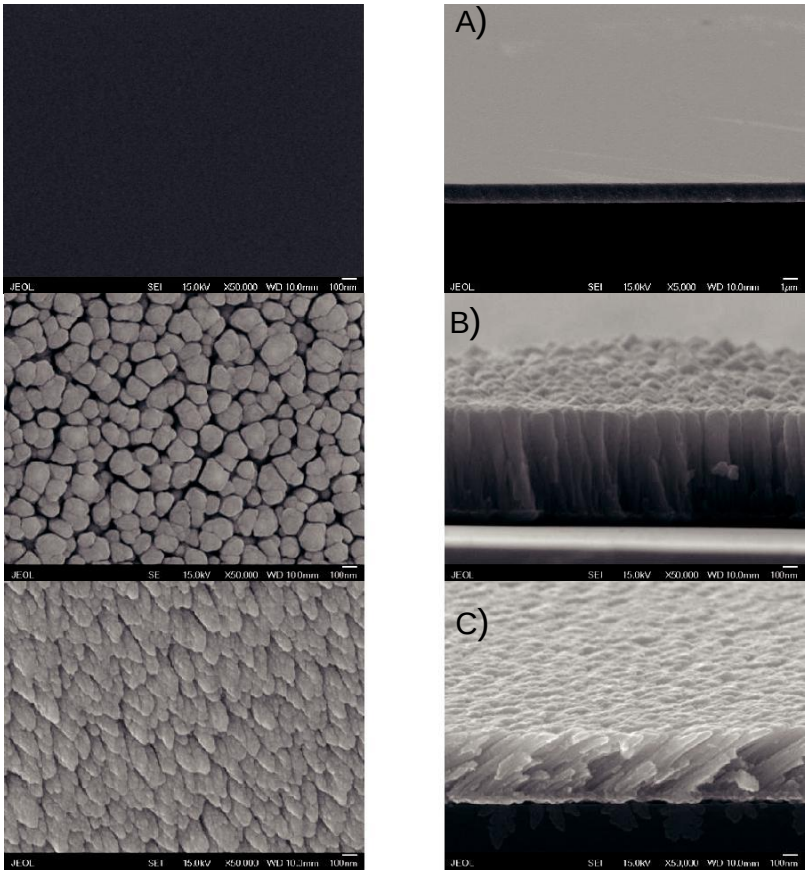

Figure 2.6. Top and cross-section scanning electron microscopy (SEM) views of (a) at Cu thin film, (b) vertical GLAD Cu nanorods, and (c) tilted GLAD Cu nanorods.

The tilted Cu nanorods deposited in the absence of substrate rotation have flat tops tilted towards the flux direction as shown in Figure 2.6(c). In addition, the slanted Cu nanorods also have a faceted top; however, many fibrous structures are present along its sidewalls in contrast to the smooth sides of the vertical Cu nanorods, indicating that the

tilted Cu nanorods are not single crystal. and the resulting nanorods had diameters as small as about 5-10 nm. As they grew longer and some of them stopped growing, due to the shadowing effect, their diameter grew up to about 100 nm. The average height of the individual rod was measured to be about 600 nm and the average gap among the nanorods also changed with their length from 5-10 nm up to 20-100 and 20-50 nm for vertical and tilted Cu nanorods, respectively, at later stages.

2.2.3 Experimental Setup

The main components constituting the cooling system are an aluminum base with 4 cartridge heaters, a nanostructured plate placed on top of it, four microchannels generating the impinging jets over the tested samples, and thin (76 µm thick) sensitive thermocouples as shown in Figure 2.7. The jet flow is in laminar region.

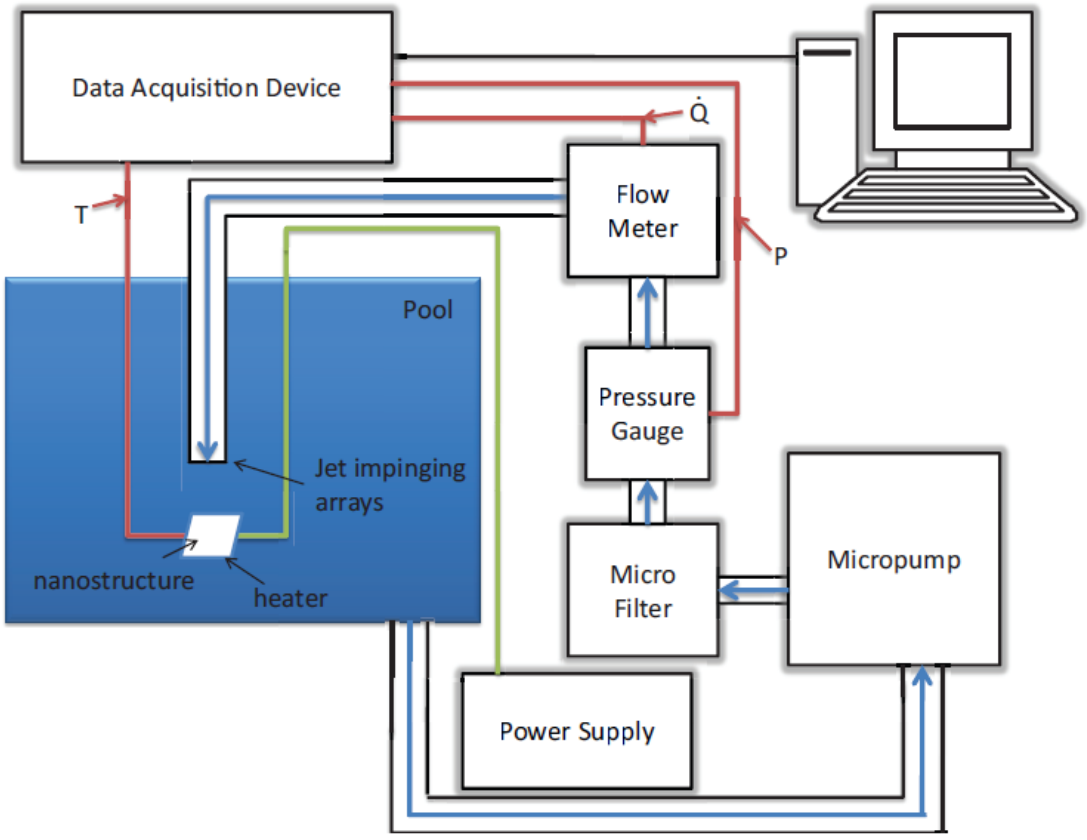

Figure 2.7. Experimental Setup.

The aluminum base of dimensions 35mmx30mmx10mm houses four built-in cartridge heaters of diameter 6.25 mm and of length 31.75 mm which are treated with a

high duty thermal grease (Omega Bond) and sealed to the base with an aluminum cap in order to enhance heat transfer rate and minimize heat losses. Four thermocouples are also treated with high duty thermal grease and attached in the gaps between each cartridge heater and the inner surface of the aluminum base as shown in Figure 2.8.

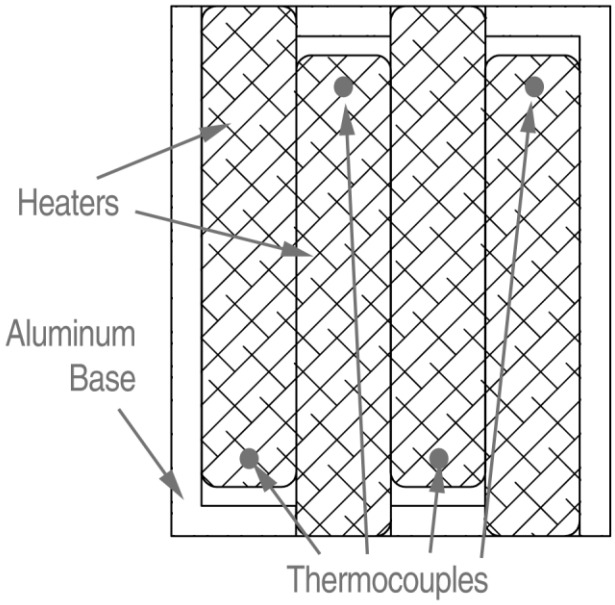

Figure 2.8. Cross section view of the heated base showing thermocouple locations.

The heaters provide constant heat flux to the system, simulating the heat generated by microchips/microprocessors. The nanostructured copper plates as well as the reference Cu thin film sample of dimensions 35mmx30mm are placed on the aluminum base. The plate is also treated with high quality thermal grease (Omega Bond) to improve the efficiency of the cooling process by enhancing the heat transfer rate. The whole setup is carefully sealed to prevent any leakages. Impinging jets are targeted to the tested surface to remove the unwanted heat away from the plate effectively. The impinging jets are provided by four microchannels of inner diameter 500 μm that are connected to the experimental setup using a high pressure sealing and have a distance of 1.5mm to the plate. DI-water is driven into the channels using a HNP Mikrosysteme micro gear pump that can be precisely tuned with a controller allowing the conduction of experiments at different steady flow rates. A Cole Parmer flow meter integrated to the system is used to measure the volumetric flow rate through the jets. To determine the pressure drop across the setup, Omega pressure gauge is attached to the inlet. Four thermocouples placed on the surface of each rod heater are used to acquire

accurate steady surface temperature data (Figure 2.8). Data is gathered through data acquisition system (NI-SCXI 1000). Data acquisition system records 100 data points per second at a 100Hz sampling rate. 12000 temperature data points were averaged for each steady state heat flux condition. These data points are then exported through data acquisition software LABVIEW after averaging via MS Visual Studio and MATLAB software once steady state conditions are reached.

2.2.4 Experimental Procedure

After the experimental setup is prepared as explained, the surface temperatures are measured as a function of the input power data gathered from the readings of the power supply. This procedure is carried out at various flow rates, which are adjusted in the inlet region of the setup. In addition to the measurements of flow rates and power values, inlet temperatures, surface temperatures, pressure drops across the system, and electrical currents flowing through the film heater were also measured with the appropriate sensors (Omega thermocouples, Omega pressure transducer, Agilent voltmeter, Cole Parmer flow meter). This procedure is then executed for the samples of vertical and tilted nanostructured plates as well as for the plain surface plate in order to investigate the effects of the nanostructured plates on heat transfer. For boiling experiments, it was made sure to set the maximum wall superheat to ~50 ^{o}C in order to protect the uniformity of the nanostructures. After the experiments, it was indeed observed that the nanostructures were not damaged.

2.2.5 Data Reduction

Heat flux provided to the system, q'', is obtained from

$$q'' = \frac{P - Q_{loss}}{A} \tag{20}$$

where P is the power input, Q_{loss} is the thermal and electrical power loss and A is the heated area of the plate. The surface temperatures are calculated by considering thermal contact resistances from the thermocouple to the surface of the nanostructured plate.

$$T_s = T_{th} - qR_{tot} \tag{21}$$

where T_{th} is the thermocouple temperature reading and R_{tot} is the total thermal resistance from the thermocouples to the surface of the nanostructured plate. The average of the surface temperatures are taken to obtain the average surface temperature T_{th}. The heat transfer coefficient, h, is then calculated by

$$h = \frac{q''}{T_s - T_i} = \frac{q''}{\Delta T} \tag{22}$$

where T_s is the surface temperature and T_i is the inlet fluid temperature. Nusselt number, Nu, is extracted from

$$Nu = \frac{hNd_i}{k} \tag{23}$$

where d_i is the inside diameter of each nozzle and N is the number of jets, k is the thermal conductivity of the fluid. The velocity, u, is expressed as

$$u = \frac{\dot{Q}}{A_c} \tag{24}$$

where $\dot{Q}$ is the flow rate of the water and A_c is the total cross-sectional area of nozzles. Jet Reynolds number, Re_j, is given as

$$Re_j = \frac{ud_i}{\nu} \tag{25}$$

where ν is the kinematic viscosity of the working fluid.

Two correlations were used in order to compare the current experimental data to previous studies. For single-phase data, Martin [80] correlation for multiple circular submerged jets is used:

$$\frac{Nu}{Pr^{0.42}} = \left(1 + \left(\frac{S_{NP}\sqrt{\alpha_j}}{0.6d}\right)^6\right)^{-0.05}\left(\frac{2\sqrt{\alpha_j}(1-2.2\sqrt{\alpha_j})}{1+0.2(S_{NP}/d-6)\sqrt{\alpha_j}}\right)(0.5Re_j^{2/3}) \tag{26}$$

where $\alpha_j = (\pi d^2)/4A_{corr}$ and A_{corr} is the area corresponding to a single jet, S_{NP} is the nozzle-to-target distance and Pr is the Prandtl Number.

For two-phase data, Chien and Chang [40] correlation was employed:

$$Nu = 2.167 Re_j^{0.67} Bo^{0.2754} (S/d)^{-0.667} \gamma_A^{0.4} \quad (27)$$

where Bo is the Boiling Number, S is the jet spacing in mm and γ_A is the surface area enhancement ratio (taken as 1 for flat plate approximation).

2.2.6 Uncertainty Analysis

The uncertainty in the measured values are given in Table 2.3 and are obtained using the propagation of uncertainty method suggested by Kline and McClintock [81].

Table 2.3. Uncertainty figures in data.

Uncertainty	Error
Power	$\pm 0.15W$
Nozzle Diameter	$\pm 0.002mm$
Temperature	$\pm 0.1\,^{\circ}\mathrm{C}$
Volumetric Flow Rate	1%
Surface Area	0.44%
Nozzle Area	1.13%
Heat Flux, Single Phase	1.28%
Heat Flux, Two Phase	3.46%
Heat Transfer Coefficient, Single Phase	5.86%
Heat Transfer Coefficient, Two Phase	8.4%
Nusselt Number, Single Phase	6.26%
Nusselt Number, Two Phase	8.72%
Flow Velocity	1.39%
Reynolds Number	1.43%

2.3 Experimental Setup and Procedure for Pool Boiling Study

2.3.1 Nanostructure Deposition

Single crystal p-type (100) oriented silicon wafers at resistivity 1-100 Ω·cm were cleaned by standard RCA-I cleaning procedure. Samples were dipped into ammonium hydroxide and hydrogen peroxide solution (NH_4OH, 30% v. : H_2O_2, 30% v. : H_2O = 1 : 1 : 5) at 80^{o}C for 15 minutes, rinsed with deionized water and dried with nitrogen gas. Following the cleaning step, single layer hexagonally close-packed polystyrene (PS) nanospheres were deposited onto samples through convectional self-

assembly method [82] and slightly etched in oxygen plasma. Plasma etching decreased nanosphere diameter from 1010 nm to 850 nm and formed a hexagonal pattern of isolated nanospheres. These non-closely packed nanospheres were used as shadow mask for gold film deposition of 50 nm thickness where gold atoms filled the gaps among nanospheres. This step was followed by nanosphere lift-off by ultra-sonicating samples in toluene for 1 minute, which left a honeycomb patterned gold mesh layer on the silicon substrate. After the patterning process, samples were immersed into room temperature hydrofluoric acid - hydrogen peroxide solution (HF, 50% v. : H_2O_2, 30% v. : H_2O = 4 : 1 : 5). Silicon underneath the gold layer etched and formed well-ordered single crystalline silicon nanowires. Samples were etched for 40 seconds, 80 seconds, and 160 seconds in order obtain Si wires of 900 nm, 1800nm and 3200 nm lengths, respectively. Finally, gold layer was removed by etching with potassium iodine (KI) solution for 3 minutes. In this metal-chemical assisted etching (MaCE) procedure, silicon nanowire diameter is defined by the reduced nanosphere diameter, nanowire separation by initial nanosphere diameter, and nanowire length is set by etching time. Effects of silicon wafer crystal orientation, etching solution concentration, and etching time on nanowire morphology were discussed elsewhere [83].

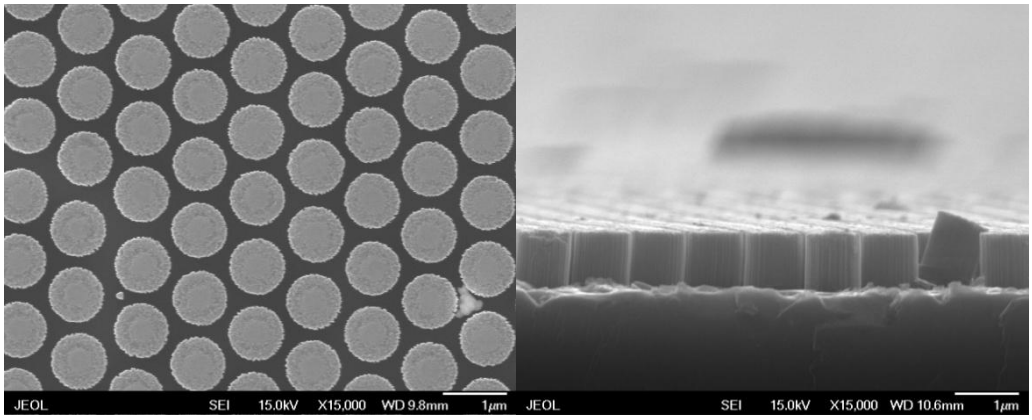

Figure 2.9. Top-view and crossectional view SEM images of single crystalline silicon nanowires after 40 seconds etching.

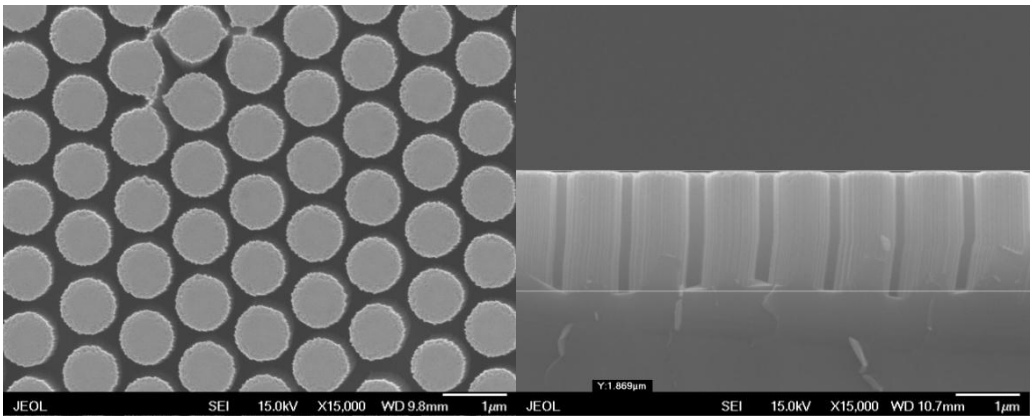

Figure 2.10. Top-view and crossectional view SEM images of single crystalline silicon nanowires after 80 seconds etching.

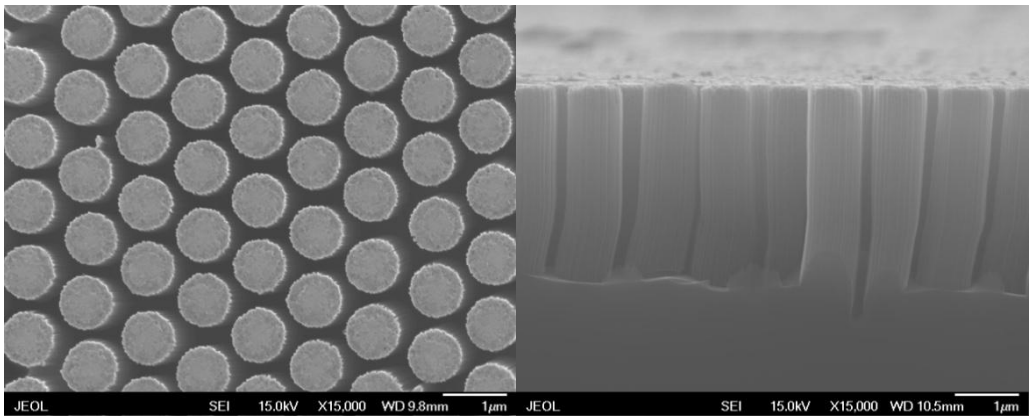

Figure 2.11. Top-view and crossectional view images of single crystalline silicon nanowires after 160 seconds etching.

2.3.2 Contact Angle Measurements

Water drop contact angle measurements of the various nanostructured nano plates using DSA (Drop Shape Analysis) are shown in Figure 2.12. Contact angle values are 74.4^{o}, 72.1^{o}, 66^{o} and 57.7^{o} for plain, 3200 nm, 1800 nm and 900nm nanorods, respectively. Namely, contact angle increases as length of the nanorods increase, however still lower than that of plain surface.

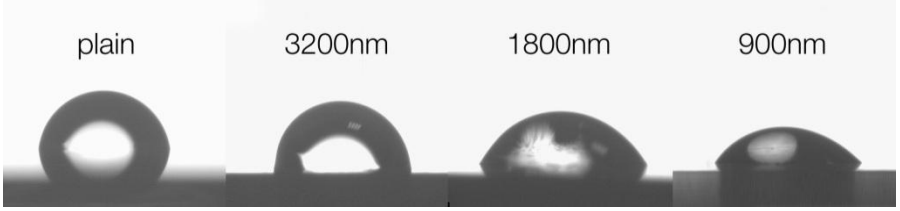

Figure 2.12. DSA images showing contact angle views for all four nanostructured nano plates.

2.3.3 Experimental Apparatus

The experimental design is demonstrated in Figure 2.13. An aluminum base of dimensions 6cmx6cm is designed such that it features a housing for four cartridge heaters, each of length 31.25 mm and of diameter 6.25 mm, which is surrounded with air gaps on all sides to minimize heat loss. On the surface of the aluminum base lies a pool of dimensions 2cmx2cm which has a depth of 4mm. A container made of Plexiglas is closely fitted to the aluminum base; hence the total depth of the pool increases to 8 mm. The heat generated by the cartridge heaters is delivered to the nanostructured plate of size 19mmx19mm that is placed on the bottom of the pool. Heaters provide constant heat flux to the system since constant voltage is applied to the ends of the heaters. Total resistance of the heaters is 65 ohms and each heater alone is capable of reaching powers as high as 225 W. The heaters and the nanostructured plate are treated with high quality silicone thermal grease in order to minimize thermal contact resistances and heat losses. The container is filled with 154.45 ml DI-Water and the water level is 5.8 cm above the nanostructured plate. One thermocouple is placed between the nanostructured plate and the bottom of the pool to record surface temperature, whereas another thermocouple is secured under the base in order to determine the heat loss.

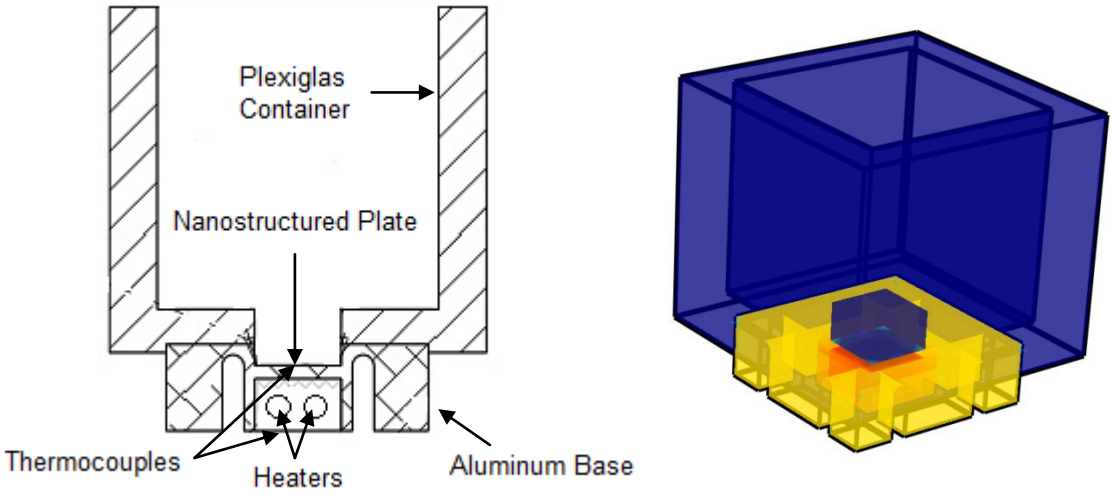

Figure 2.13. Experimental setup section view and 3D representation.

2.3.4 Experimental Procedure

After the experimental setup is prepared as explained, the surface temperature is measured (through OMEGA thermocouples) as a function of the input power calculated using voltage and current readings on the power supply (AMETEK Sorensen XHR Series Programmable DC Power Supply). Surface temperature is recorded for various constant heat flux values. Temperature data are recorded with the aid of a computer integrated data acquisition system (NI-SCXI 1000) at a rate of 100 data points per second. These data points are exported using data acquisition software LABVIEW and then averaged using MS Visual Studio and linearized using MATLAB.

Constant voltage is applied to the ends of the cartridge heaters (Isitel Cartridge Heaters) providing constant heat flux to the surface. Heat flux values covered a range that includes both single phase and boiling heat transfer conditions. The experiment is repeated for each of the four plates, three of them featuring Si nanowires of different lengths and one being plain surface Si control sample. The results are compared to characterize the effects of nanostructures on boiling heat transfer performance of the cooling system designed.

2.3.5 Data Reduction

Heat flux provided to the system, q", is obtained from

$$q" = \frac{P - Q_{loss}}{A} \tag{28}$$

where P is the power input, Q_{loss} is the thermal and electrical power loss and A is the heated area of the plate. The surface temperatures are calculated by considering thermal contact resistances from the thermocouple to the surface of the nanostructured plate,

$$T_s = T_{th} - q" * R_{tot} \tag{29}$$

where T_{th} is the thermocouple temperature reading and R_{tot} is the total thermal resistance from the thermocouples to the surface of the nanostructured plate. The average of the surface temperatures are taken to obtain the average surface temperature T_{th}. The boiling heat transfer coefficient h, is then calculated by

$$h = \frac{q''}{T_s - T_{sat}} \quad (30)$$

Where T_s is the surface temperature and T_{sat} is the saturation temperature of the fluid. T_{sat} is replaced with T_i while calculating single phase region heat transfer coefficient, which is the initial temperature of the liquid pool.

2.3.6 Uncertainty Analysis

The uncertainties of the measured values are given in Table 2.4 and are derived from the manufacturer's specification sheet while the uncertainties of the derived parameters are obtained using the *propagation of uncertainty* method developed by Kline and McClintock [81].

Table 2.4. Uncertainty analysis results.

Uncertainty	Error
Power (P)	±0.15 W
Surface Area (A)	±0.08 %
Thermocouple Reading (T_{th})	±0.1ºC
Thermal Resistance (R_{tot})	5 %
Heat Transfer Coefficient (h)	9 %
Contact Angle	±0.1º

3 RESULTS AND DISCUSSION

3.1 Results and Discussion of Micro Pin Fin Heat Sink Study

3.1.1 Validation Runs

The 2CLD (circular less dense pin fin) micro pin-fin heat sink device from the experiments of Koşar and Peles [17] is exactly modeled (including the heat transfer within the micro pin-fins) for validation purposes. Experimentally applied pressure drop (ΔP) and heat flux (q) are taken as the input parameters. The results were obtained over Reynolds numbers ranging from 14 to 720.

Figure 3.1 depicts the temperature distribution along the channel and at the mid height of the channel. The minimum and maximum temperatures are represented by dark blue and red colors, respectively. The left side wall of the micro channel has an

increasing temperature (which finally reaches a global maximum) as it gets closer to the outlet. Due to the symmetry plane at the right of the channel, the flow on the right plane does not have a zero velocity as it is on the left, and thus, it has a lower temperature gradient through the channel.

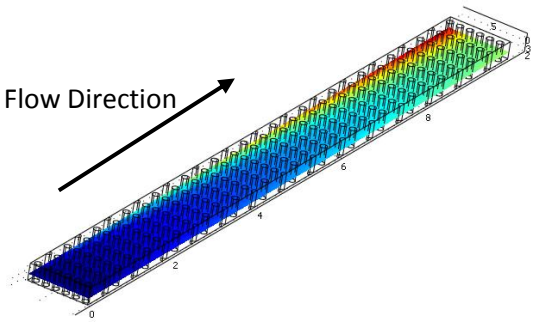

Figure 3.1. Temperature distribution of the numerical model of 2CLD device from the experiments of Koşar & Peles **[17]**

In order to show the agreement between the validation model and experimental results, the surface averaged heated base temperatures (the total area of pin-fin cross sections is subtracted from the base area of the channel and total surface area of pin-fins is added) are plotted against applied heat fluxes for the two fixed pressure drops. Figure 3b proves the strong agreement between numerical and experimental results. The corresponding maximum error percentages (between experimental and numerical surface temperatures) for ΔP=36.8 and 20.3 kPa are 13% and 7%, respectively.

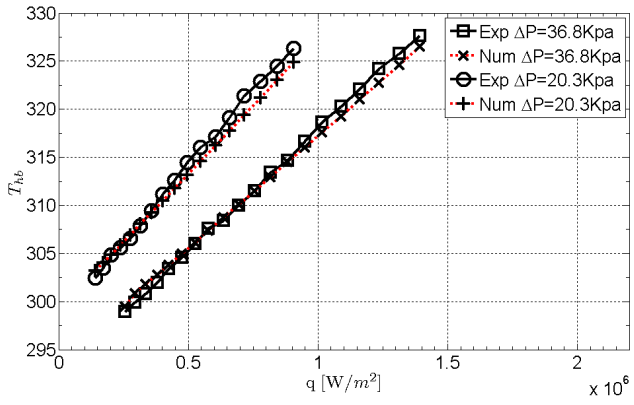

Figure 3.2. Comparison between numerical and experimental surface averaged temperatures for the heated base of the micro channel in cases of varying pressure differentials

3.1.2 Simulations of pin-fins with different cross sections

The applied boundary conditions are verified for the hydrofoil pin-fin geometry at *Re*=20 in Figure 3.3 and Figure 3.4 as samples. Figure 4a shows slices of *u* (velocity component normal to inlet surface) values, which range from 0 to 0.354 m/s or dark blue to red on the color legend. At the right of the channel, the vertical plane is the symmetry plane, and its boundary condition is applied by having a non-zero velocity values everywhere on its surface.

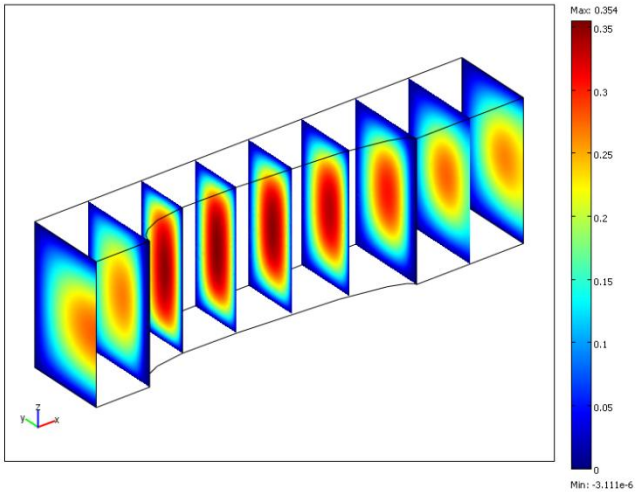

Figure 3.3. Normal to inlet surface velocity, *u* slices for the hydrofoil pin-fin heat sink with *Re*=20 condition.

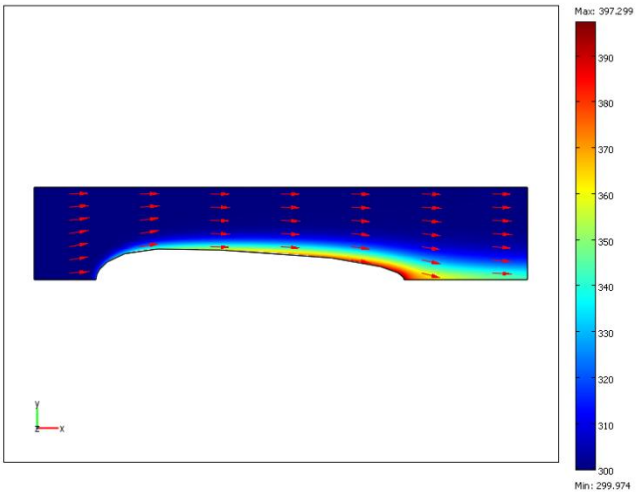

Figure 3.4. Temperature slice transaction in the middle of length on the z-direction of the heat sink and velocity arrows for the hydrofoil heat sink with *Re*=20 condition.

Figure 3.4 shows the temperature distribution slice taken from the mid height of the micro channel and the normalized velocity arrows. The temperature distribution ranges from 300 to ~397 K or from dark blue to red on the color legend. The temperature at the inlet is 300 K everywhere. The temperature rise starts at the upstream point of the hydrofoil, and the heated fluid layer gets thicker as it gets closer to the outlet. The velocity arrows are always parallel with the hydrofoil surface, and no flow separation is observed downstream the hydrofoil shaped pin fin.

Figure 3.5, Figure 3.6 and Figure 3.7 show the importance of the pin-fin shape on flow separation by depicting the streamlines and temperature slices of circular, cone, diamond, hydrofoil, rectangular, square and triangular shaped micro pin-fins. At a Reynolds number of 20, there is an apparent flow separation particularly downstream the triangular, circular, rectangular and square pin-fin, whereas flow separation is absent at cone, diamond and hydrofoil shaped pin-fins. Sharp corners of triangular, rectangular and square pin-fins trigger flow separation and enhances wake region that leads mixing close to the edge of the pin-fins. Besides, there is also a wake region at the circular shaped pin-fin even though it has no sharp corner.

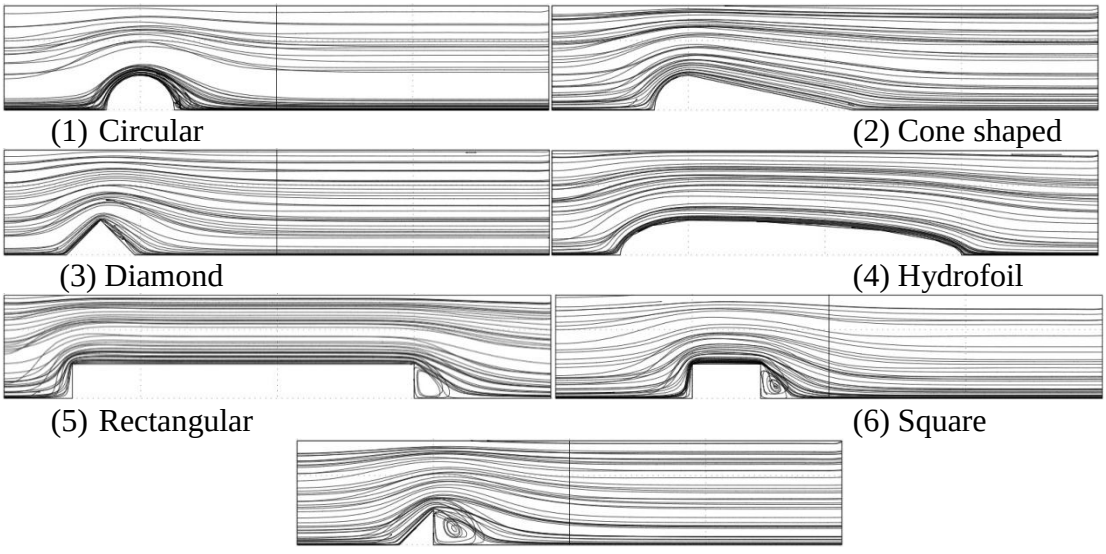

Figure 3.5. Transactions of the flow streamlines of various micro pin-fin geometries from the cross section taken at the mid height level at *Re*=20.

Figure 3.6 shows that increasing Reynolds number to 50 leads to more pronounced flow separation for the circular, rectangular, square shaped and triangular pin fins. Increased Reynolds number promotes flow separation that leads to a larger

wake region downstream the pin-fins. Besides, flow separation starts to appear on the surface of the diamond shaped pin-fin.

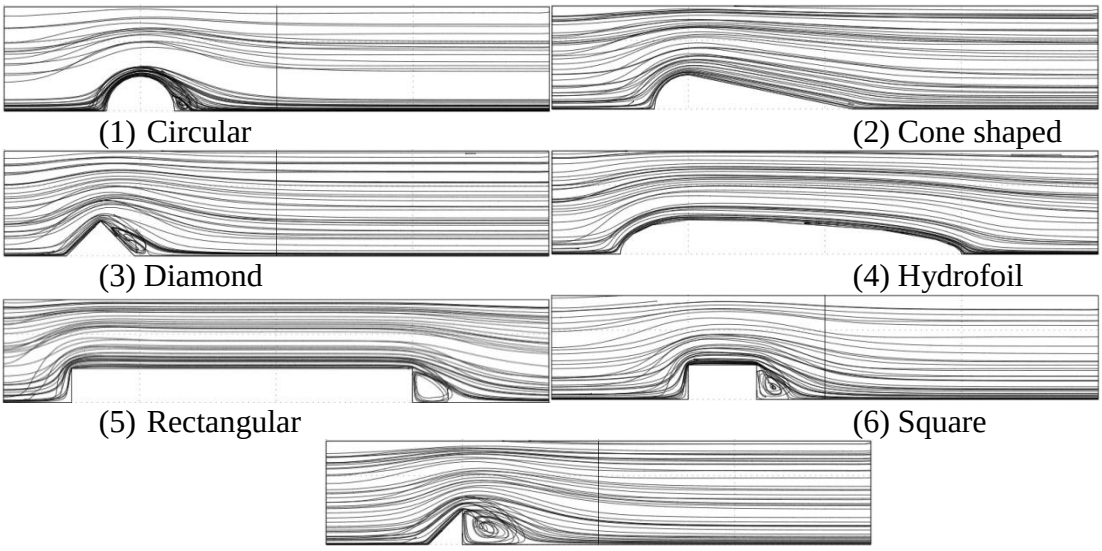

Figure 3.6. Transactions of the flow streamlines of various micro pin-fin geometries from the cross section taken at the mid height level at *Re*=50.

Figure 3.7 shows the flow over various micro pin-fins at Reynolds number of 100. All flows except the flows over cone shaped and hydrofoil shaped pin-fins experience flow separation that causes mixing and wake appearance downstream the pin-fins. Compared to the Reynolds number of 20 and 50, there are larger wake zone and more pronounced separation around pin-fins leading to a better mixing. The length of the wake zone corresponds to circular, diamond, rectangular, square and triangular pin fins is $3x10^{-5}$, 0, $5.5x10^{-5}$, $4x10^{-5}$ and $7x10^{-5}$ m at *Re* of 20, while it enhances to $4.5x10^{-5}$, $4x10^{-5}$, $8x10^{-5}$, $6x10^{-5}$ and $9x10^{-5}$ m at *Re* of 100, respectively. It can be seen that this zone is broader for the triangular micro pin fin compared to the others implying pronounced flow separation in this geometry. A fixed pair of symmetric vortices is apparent for all the micro pin fin configurations promoting flow separation, whereas laminar vortex streets cannot be observed in any of the configurations. For a 2-D flow over a cylinder symmetric steady vortices are present for *Re* between 5 and 40, while laminar vortex streets are identified for *Re* between 40 and 200 [84, 85]. The absence of laminar vortex streets for *Re* of 50 and 100 in the flow separation promoting micro pin fin geometries could be associated with the flow stabilization effects of endwalls in micro pin fins having intermediate height to diameter ratios (Figure 3.8) [15].

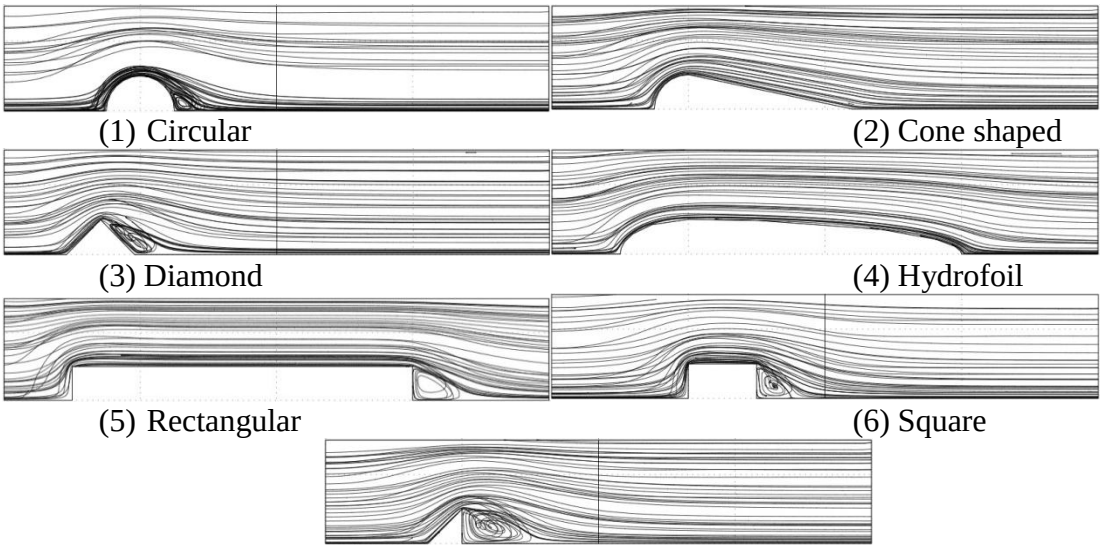

Figure 3.7. Transactions of the flow streamlines of various micro pin-fin geometries from the cross section taken at the mid height level at *Re*=100.

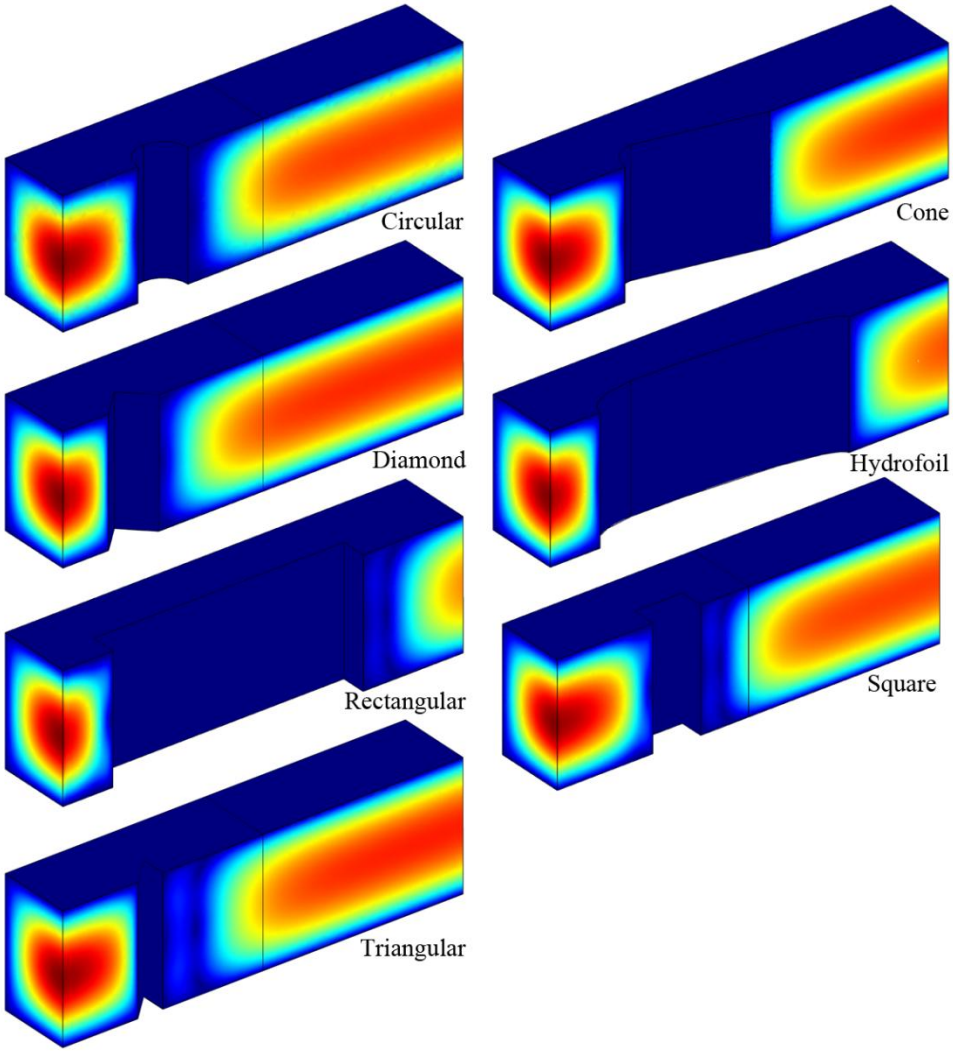

Figure 3.8. Velocity boundary layers at Re = 20.

The effects of the end walls are presented as velocity profiles at Reynolds number of 20 in Figure 3.8. The penetration lengths of endwalls effects for the circular, diamond, rectangular, square and triangular shaped pin fins are about 10^{-4} m along the pin fin surfaces, and are greater than those of cone and hydrofoil shaped pin fins', which could be due to the contribution of sharp corners to the pin fin and channel top/bottom wall interactions.

Figure 3.9 demonstrates heat transfer coefficients for various pin-fin shapes. The rectangular pin-fin has the highest *h* over the whole mass flow rate range. It has a 9% higher performance than its closest successor hydrofoil shaped pin fin. For all the profiles, heat transfer coefficient *h* increases with mass flow rate. The performances (based on heat transfer coefficient, from higher to lower) of other micro pin-fins are in the order of cone, triangular, square, diamond and circular shapes.

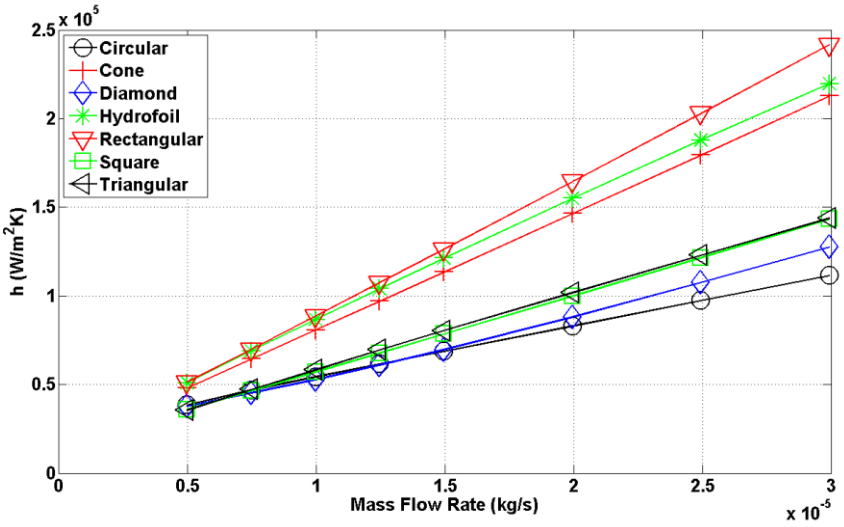

Figure 3.9. Average heat transfer coefficient, *h*, as a function of Mass Flow Rate.

Moreover, the extent of *h* dependency on mass flow rate is affected by the micro pin-fin shape. This dependency of the rectangular shaped profile is stronger than the rest of the profiles. Micro pin fins with sharp pointed regions trigger separation effects, which cause an increase in the heat transfer and mixing of the fluid [17]. Moreover, the rectangular pin fin configuration has a larger surface area compared to circular, triangular, square and diamond pin fin shape configurations. Higher heat transfer coefficients in the hydrofoil shaped pin fin compared to cone shaped, triangular, square, diamond and circular pin fins display significant effect of enhanced area on heat transfer

under the conditions in the current study. Rectangular shaped model has both sharp pointed regions and larger surface area, which leads to the highest heat transfer performance among all the micro pin fin shapes (Figure 3.5, Figure 3.6, Figure 3.7) [84]. For flow separation promoting pin fin shapes (Figure 3.5, Figure 3.6, Figure 3.7), the triangular configuration generating a larger wake zone downstream the micro pin fin results in higher heat transfer coefficients compared to square, diamond and circular micro pin fins.

Figure 3.10 shows Nusselt number *Nu* profile as a function of Reynolds number *Re*. Re range is selected in parallel lines to the *Re* values in experimental studies on micro pin fins [15]. *Nu* and *h* profiles have the similar trends. It can be observed that the rectangular pin-fin has the highest Nusselt number over the whole *Re* range followed by hydrofoil and cone shaped micro pin fins with larger surface areas. The performances of circular and diamond pin-fins are closer for *Re* lower than 70. This result agrees with the literature since they were proposed to be interchanged for practical uses by [22] due to their similar *Nu* performances demonstrated in millimeter scale experiments.

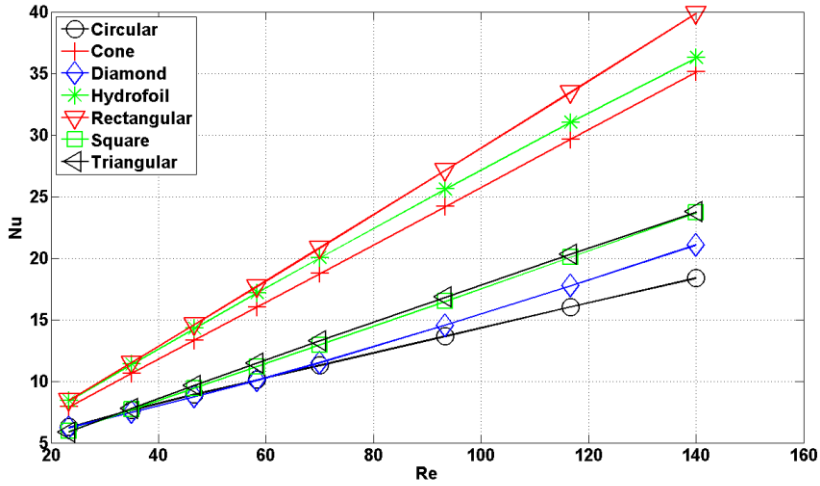

Figure 3.10. Nusselt, *Nu,* as a function of Re.

Figure 3.11 shows pressure drop, *ΔP,* as a function of mass flow rate. It can be observed that the rectangular pin-fin has the largest pressure drop over the whole mass flow rate range. Sharp points in the geometry have a significant effect on the larger pressure drop because of the form drag. As shown in Figure 3.11, pin fins with sharp edges such as rectangular and square shaped pin fins have larger pressure drop. However, the hydrofoil shaped pin fin has a larger pressure drop even though it does not

have any sharp points. Sharp pointed regions cause form drag, which can be seen in rectangular, diamond, triangular and square shaped models, while larger surface area results in more friction drag. In this point of view, the effect of larger surface area can be seen as a trigger of the larger pressure drop due to the friction drag [84]. In total, form drag and friction drag effects lead to the largest pressure drop for the rectangular shaped micro pin fin. Besides, friction drag imposed by the hydrofoil shaped micro pin fin seems to have a more dominant effect on pressure drop than the form drag generated by the square micro pin fin.

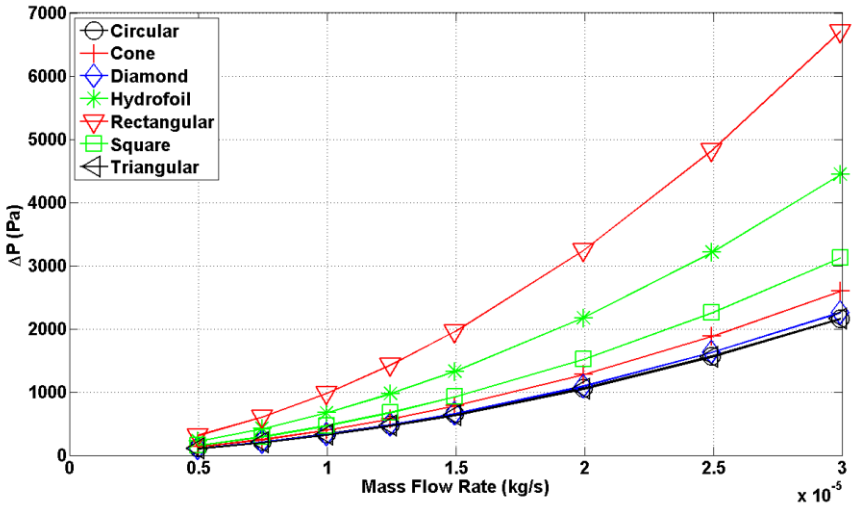

Figure 3.11. Pressure Drop, *ΔP,* as a function of *Mass Flow Rate.*

Figure 3.12 shows friction factor, *f,* as a function of *Re*. It can be observed that the rectangular micro pin-fin has the highest friction factor over the whole *Re* range, which is followed by hydrofoil, square, cone, circular, diamond, and triangular shaped pin-fins, respectively. Besides, the values of friction factor of rectangular shaped pin fin agree with the study of Bilen et al. [86] on finned surfaces. The results reflect the effects of the shape and surface area on the friction factor. Rectangular pin fin configuration generates higher friction factor due to the increased form drag because of its sharp points and flow separation (Figure 3.5, Figure 3.6, Figure 3.7) and also due to the increased friction drag because of its large surface area. Both form drag and friction drag are significant over the Reynolds number range in the current study.

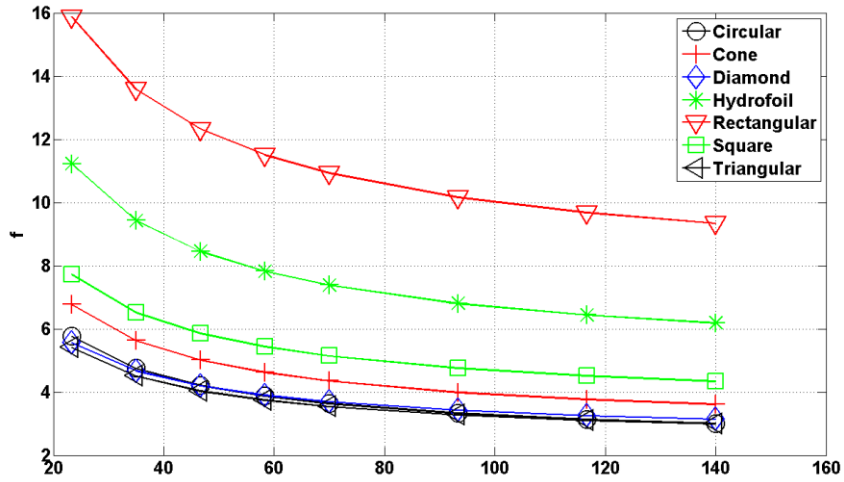

Figure 3.12. Friction factor, *f*, as a function of *Re*.

Figure 3.13 shows thermal performance index (TPI) based on circular pin fins, η, as a function of Re. Cone shaped micro pin fin has the highest TPI over the whole Re range, which is followed by hydrofoil, rectangular, triangular, square and diamond at Re values higher than 60, respectively. At low Re values, TPI of square and diamond shaped micro pin fins is lower than their circular counterparts.

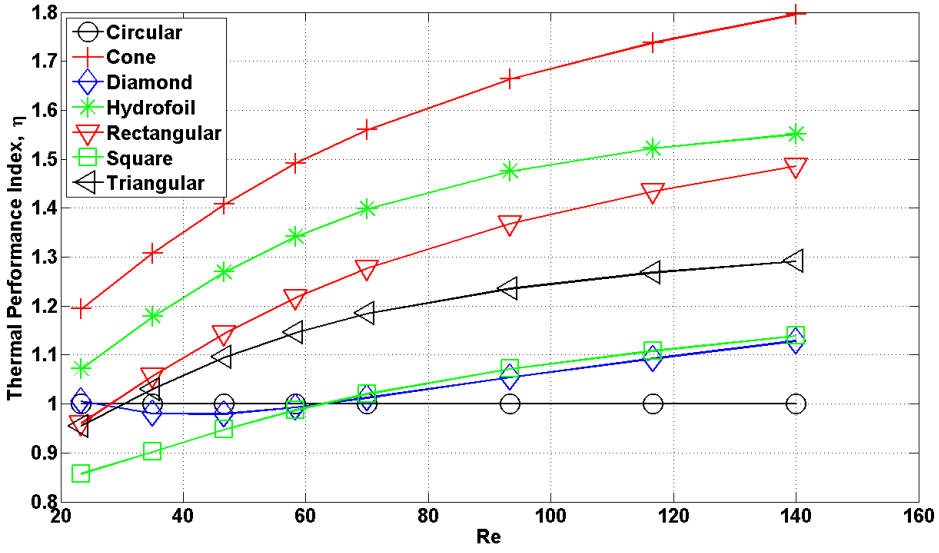

Figure 3.13. Thermal Performance Index, η, as a function of Re.

As shown in Figure 3.5, Figure 3.6 and Figure 3.7, there is no wake region appearance and flow separation for cone shaped micro pin fins and flow streamlines of cone shaped micro pin fins follow the pin fin surface, which leads to lower friction factor compared to the rectangular and hydrofoil shaped pin fins as shown in Figure 3.11 and Figure 3.12. Although Nusselt numbers and heat transfer coefficients of cone shaped micro pin fin are lower than rectangular and hydrofoil shaped micro pin fins as shown in Figure 3.9 and Figure 3.10, the effect of reduced friction factor in the cone shaped pin fin is more dominant resulting in a higher TPI value. From Figure 3.13, it could be also deduced that the use of pin fins with non-conventional shape could be attractive (a higher performance up to 80%) particularly at relatively high Re (Re>60).

3.2 Results and Discussion of Jet Impingement Study

The experimental results are obtained as explained in the previous sections. Single phase heat flux and ΔT results are plotted in Figure 3.14 for a) Re_j = 1164.6, b) Re_j = 1565.5 and c) Re_j = 1966.3. It is evident that vertical nanorods effectively remove the excess heat from the surface of the plate at all the tested flowrates, however, tilted nanorods fail to enhance heat transfer even compared to the Cu thin film coated plate. Averaged single phase heat transfer coeffcients are displayed in Fig. 6 along with Martin [80] correlation results for multiple circular submerged jets. Average heat transfer coefficient, h_{avg}, which quantities the convective heat transfer capability of a heat sink, and average Nusselt Number, Nu_{avg}, are plotted as a function of jet Reynolds number, Re_j , in Figure 3.15 Martin [80] correlation shows a fair agreement with the Cu thin film plate experimental results. The resulting mean absolute error is calculated as 13.2%. This error could be associated with the slight deviation from Martin's [80] correlation's applicable Reynolds number range. Enhanced heat transfer coefficients can be observed with the application of the nanostructured plate with vertical nanorods, whereas the nanostructured plate with tilted nanorods is proven to be less efficient even compared to the Cu thin film plate implying that the cooling performance of the jet impingement system is not promoted. An average single phase heat transfer enhancement of 22.4% has been observed with the vertical nanorods compared to the reference Cu thin film plate. The enhancement in heat transfer obtained using nanostructured plate with vertical nanorods can be attributed to the secondary flows around the nanorods and the modification of boundary layers developing from the

heated surface. Khudhayer et al.'s work [87] has shown a significant reduction in the macroscopic water contact angle of vertical metallic nanorods, implying the increased wettability because of the enhanced roughness caused by the nanorod structure, which, in turn, contributes to the enhanced heat transfer surface area. Hence, the increased heat transfer surface area available to remove heat from the surface of the base creates a more efficient cooling system. In addition, the nanorods also minimize the heat transfer resistance induced by the presence of a thin layer of the fluid on the subjected surfaces, which can be easily broken on the nanostructured surfaces compared to plain surfaces, thereby further contributing to heat transfer. As explained in the previous SEM images (Figure 2.6(b)), vertical nanorod arrays form a very rough surface increasing the contact area with water and thus enhance the heat transfer. Moreover, single crystal structure of individual nanorods is believed to further enhance the heat transfer properties of the nanostructure plate. On the other hand, the reason for poorer heat transfer performance of the nanostructured plate with tilted nanorods can be attributed to the decreased supply of liquid jets to the base of the plate due to the tilted orientation of the nanorods, which have smaller gaps compared to the vertical nanorods. This may cause the liquid to be in contact with only the tops of the tilted Cu nanorods which in turn results in poorer heat transfer rate due to the decreased heat transfer surface area and the increased resistance to heat transfer which originates from the air gaps among the tilted nanorods. Moreover, the low heat transfer of tilted nanorods might be also attributed to the non-single crystal property of these nanorods which decreases heat transfer and also enhances the surface oxidation. The surface oxidation can greatly decrease the thermal conductivity. However, the vertical nanostructure arrangement with larger gaps and vertical orientation allows liquid jet supply to the base, which significantly enhances the liquid-solid contact area and improves the heat transfer.

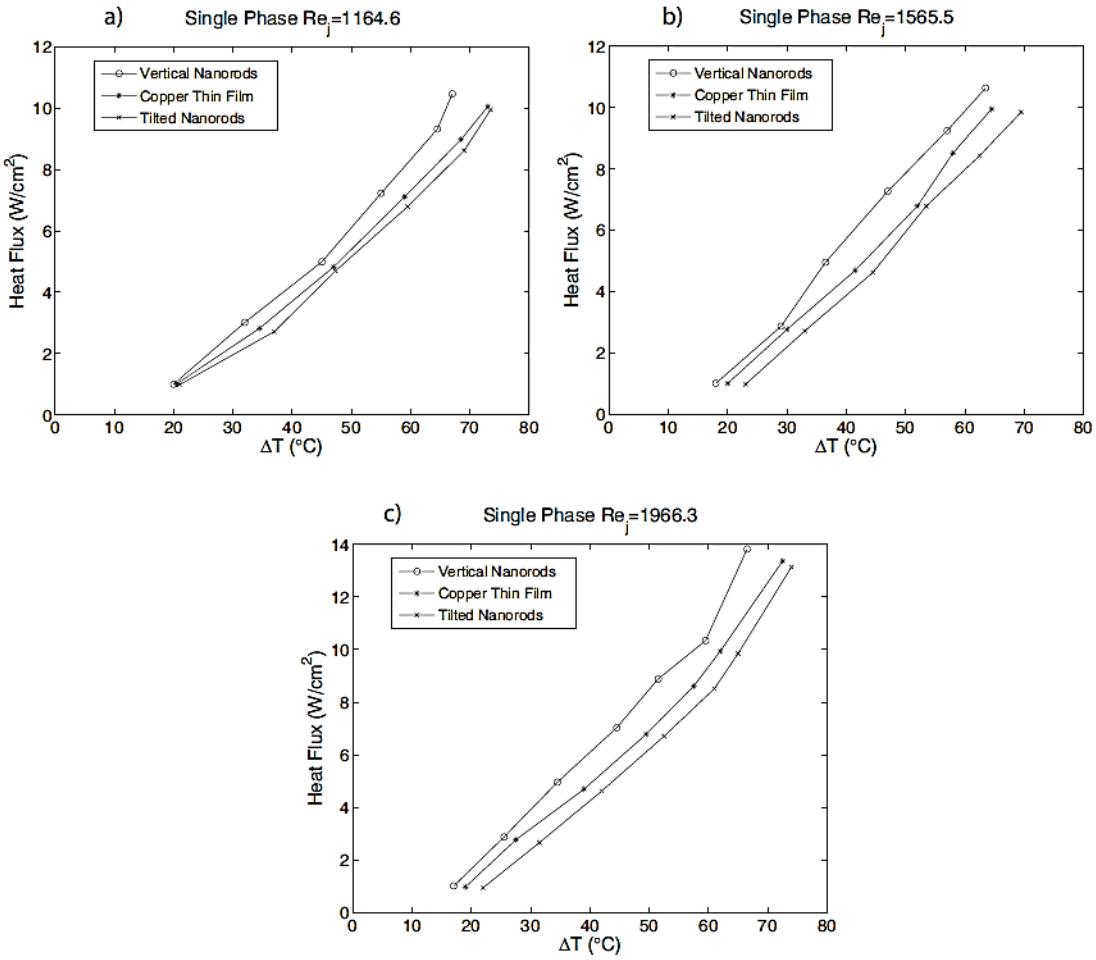

Figure 3.14. Single phase heat flux plotted with a) T at Re_j = 1164.6, b) T at Re_j = 1565.5 and c) T at Re_j = 1966.3.

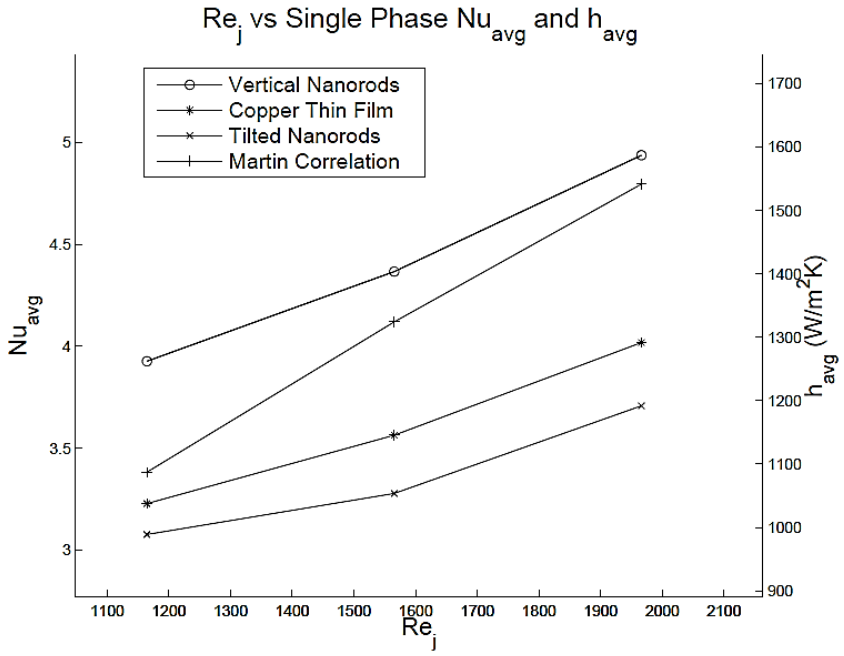

Figure 3.15. Jet Reynolds number plotted with average single phase Nusselt Number and heat transfer coefficient.

The results of the boiling heat transfer experiments conducted at constant volumetric flowrate of 107.5 ml/min (Re_j = 1164.6) are depicted in Fig. 7(a). The log-log plot of heat flux and T values in Figure 3.16 indicates that vertical nanorods greatly enhance the heat removal from the surface of the plate in the boiling regime. An average enhancement in heat transfer coefficient of 104.5% can be observed at this flow rate. Tilted nanorods, however, are still unable to augment heat transfer compared to the at plate configuration due to the previously discussed reasons. Figure 3.16(b) and Figure 3.16(c) display the two phase experimental results of the volumetric flow rate of 144.5 ml/min (Re_j = 1565.5) and 181.5 ml/min (Re_j = 1966.3), respectively in log-log plots. Nanostructured plate with vertical nanorods again yields the best results at these flow rates. Average enhancements in heat transfer coefficients of 96.8% (Re_j = 1565.5) and 68.6% (Re_j = 1966.3) have been achieved compared to the plain surface, while the tilted nanorod structure results in the lowest performance similar to the lower flowrate results.

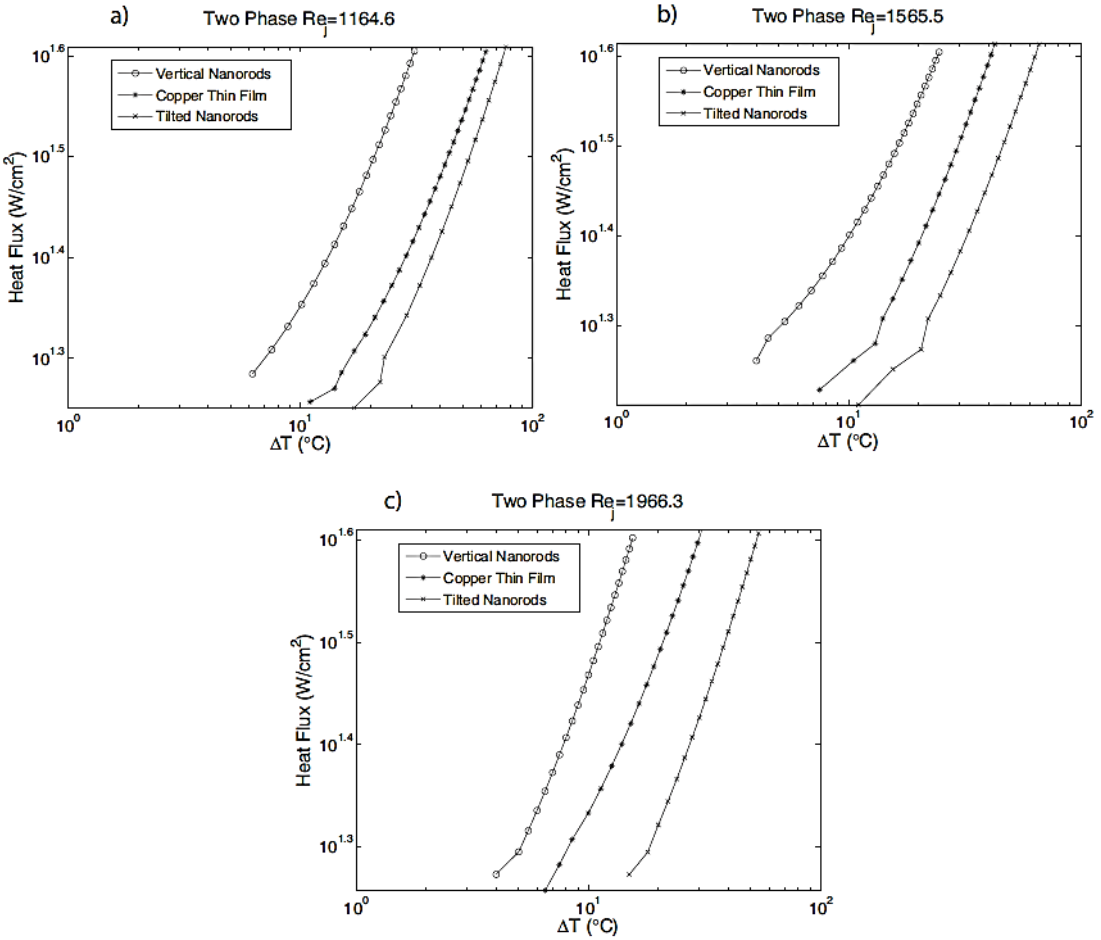

Figure 3.16. Two phase heat flux plotted with a) *T* at Re_j = 1164.6, b) *T* at Re_j = 1565.5 and c) *T* at Re_j = 1966.3.

Average heat transfer coefficients and mass fluxes for two phase experimental data are displayed in Figure 3.17 for three different flow rates along with Chien and Chang [40] correlation results. In these Figures, a significant increase in heat transfer coefficient with the nanostructured plate based on vertical nanorods is apparent. An average two phase heat transfer enhancement of 85.3% has been observed with the vertical nanorods compared to the reference Cu thin film plate. Heat transfer coefficients are greater for higher flow rates when compared to the lower flow rates. This result indirectly implies that Nusselt number has a strong dependence on Reynolds number, which has been also extensively reported in the literature [88]. At higher flow rates, heat transfer coefficients exceeding $30000 W/m^2K$ are observed with the nanostructured surfaces for the proposed cooling device, which is promising. Chien and Chang [40] correlation agrees with the Cu thin film results significantly. The resulting mean absolute error is calculated as 5.5%. Chien and Chang [40] correlation's applicability range is well within the scope of this study, which is the reason for the good agreement between the correlation and the experimental study.

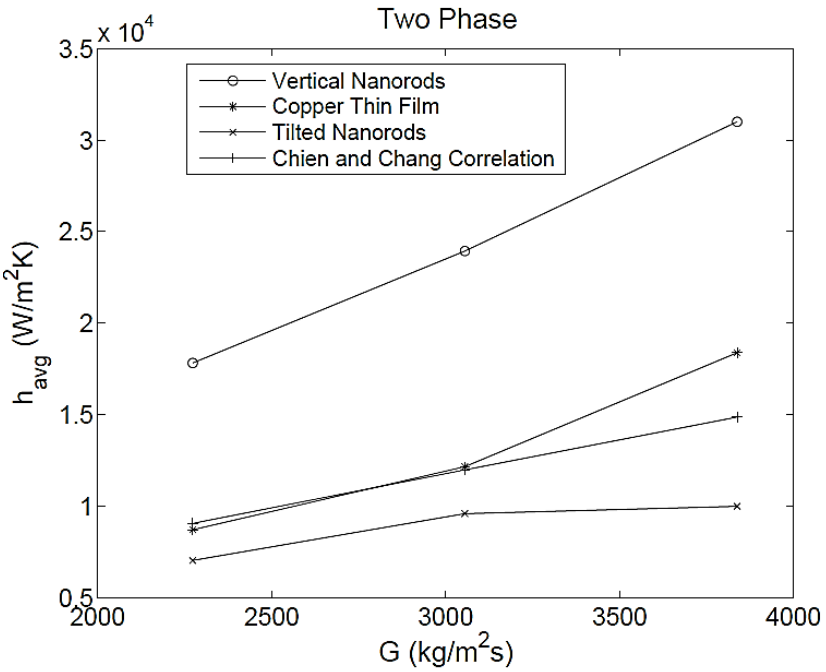

Figure 3.17. Two phase heat transfer coefficient average vs mass flux.

The enhanced heat transfer performance obtained from the nanostructured surface with vertical nanorods in jet impingement agrees with the previous experimental studies [45] and results on nanostructured surfaces used with other heat transfer modes in the literature [43, 54]. Previously, pool boiling and single phase flow in rectangular channels with nanostructured surfaces were investigated and significant enhancements in heat transfer were reported [41, 42]. Positive effects of the nanostructured surfaces with sparsely spaced tilted nanorods have been reported in boiling applications [54], but studies on the performance of such surfaces in jet impingement applications are not present in the literature. The experimental results reported in this study show that tilted nanorods, when densely packed, fail to enhance heat transfer with jet impingement applications, and thus, the heat transfer performance of the system is decreased. On the other hand, well-spaced vertical nanorods with a better exposure to the liquid results in an enhanced heat transfer performance, especially in the boiling regime. The vertical nanorods act as pin fins that increase the surface roughness and hence increase the surface wettability by decreasing the contact angle. Moreover, they can augment the number of bubbles generated by increasing the number of active nucleation sites, which is triggered by multiple nanorods acting together to offer more hot spots for bubble nucleation. Although the spacing between two nanorods is below the critical active nucleate size reported in the literature, the combined spacings among multiple nanorods exceed the critical size providing additional active nucleate sites. On the other hand, tilted nanorods have drawbacks since they decrease the liquid supply to the base of the plate, where the temperature is the highest. Their denser structure introduces another source of thermal resistance, leading to a further decrease in the heat removal performance. Moreover, the configuration of the tilted rods generates blockage for bubble departure due to their non-vertical orientation thereby decreasing nucleate boiling heat transfer.

3.3 Results and Discussion of Pool Boiling Study

Experimental data is gathered as explained in the previous sections. Surface temperature data points are plotted against various constant heat flux values between 0.3 W/cm^2-23 W/cm^2 for all four plates and presented in Figure 3.18. Nanostructured plate with Si nanowires of length 900 nm (referred to as Si NW 900 nm in the legends) has shown the best improvement on the surface temperature compared to the plain surface Si control sample (referred to as Plain Si in the legends). Surface temperature at the boiling inception remained very close to 100 ºC. Other two nanostructured plates with 1800 nm and 3200 nm Si nanowires respectively (referred to as Si NW 1800 nm and Si NW 3200 nm in the legends) have shown the same trend and enhanced the heat transfer compared to the plain surface Si plate, but with a slight increase in surface temperatures. As the length of the nanowires increased, a surface temperature increased, too. This behavior is attributed to the descending wettability of the surface due to the ascending nanowire length. Overall enhancement on the heat transfer characteristics is attributed to the pin-fin [43] effect of the nanowires. The increased heat transfer surface area available to remove heat from the surface created a more effective cooling system.

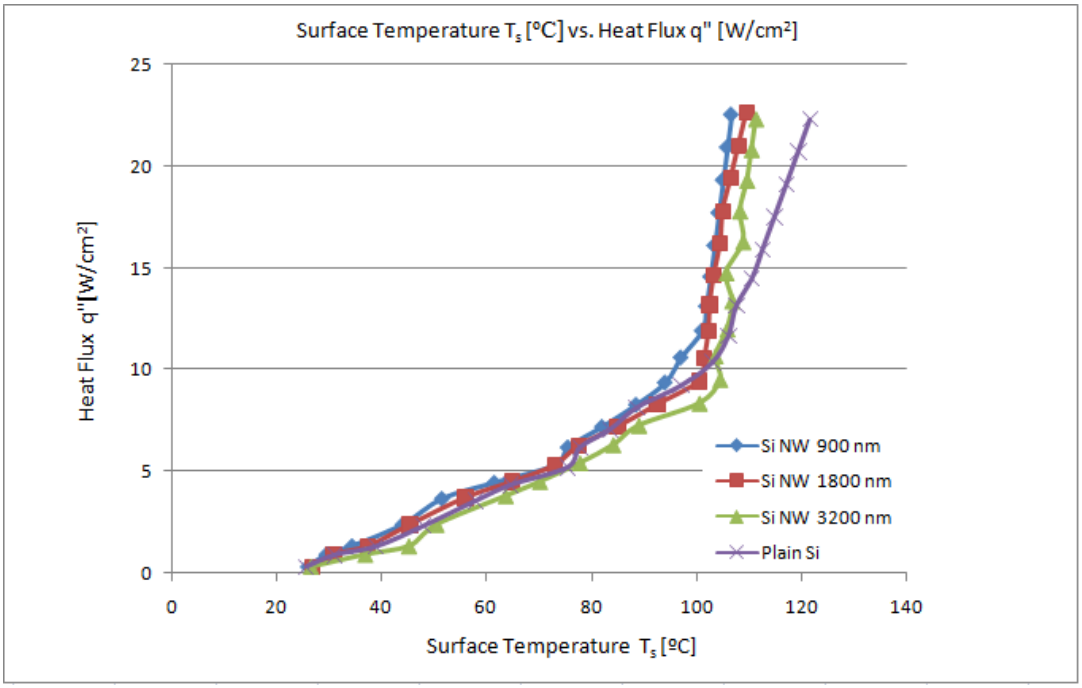

Figure 3.18. Surface temperature vs. various constant heat flux values for all test samples.

Boiling heat transfer coefficients of all four plates are plotted against various heat fluxes and presented in Figure 3.19. As expected after the temperature readings are analyzed, nanostructured plate with the shortest nanowires of 900 nm makes the greatest difference compared to the plain surface Si plate. Heat transfer coefficient average of the nanostructured plate with 900 nm nanowires is 3.5 times the average heat transfer coefficient of the plain surface Si plate in boiling region. Worst case observed using a nanostructured plate still yields a huge enhancement in average heat transfer coefficient. The nanostructured plate with Si nanowires of 3200 nm results in 2.2 times the average heat transfer coefficient of the plain surface Si plate. This positive effects can be attributed to the decreased contact angle of the liquid with heated surface [56]. Decreasing contact angle increases surface wettability [70, 64, 69, 65, 66] by increasing capillary surface forces, hence fluid flow to the nucleation sites is promoted [56]. This also yields a higher bubble generation frequency. It is also widely studied and proven that such nanostructured surfaces have the ability of increasing the nucleation site density and bubble generation frequency from the surface [89].

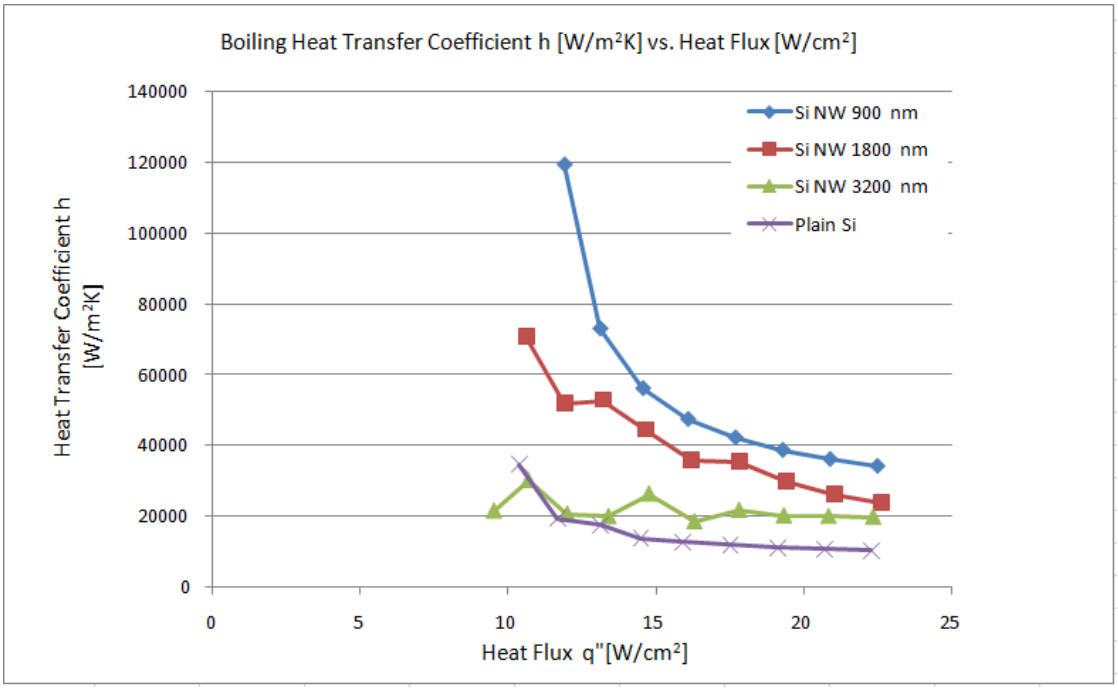

Figure 3.19. Boiling heat transfer coefficients vs. various constant heat flux values for all test samples.

Single-phase region heat transfer coefficients of the plates are plotted against various heat flux values and are presented in Figure 3.20. Nanostructured plates with

900 nm and 1800 nm Si nanowires yielded better results compared to the plain surface Si plate, whereas in single-phase region, nanostructured plate with 3200 nm Si nanowires performed the worst. This behavior can be attributed to the increasing thermal resistance due to the increasing thickness of the plate. Without the superior heat removal performance of boiling conditions, nanostructured plate with such long nanowires failed to enhance the heat removal performance of the system.

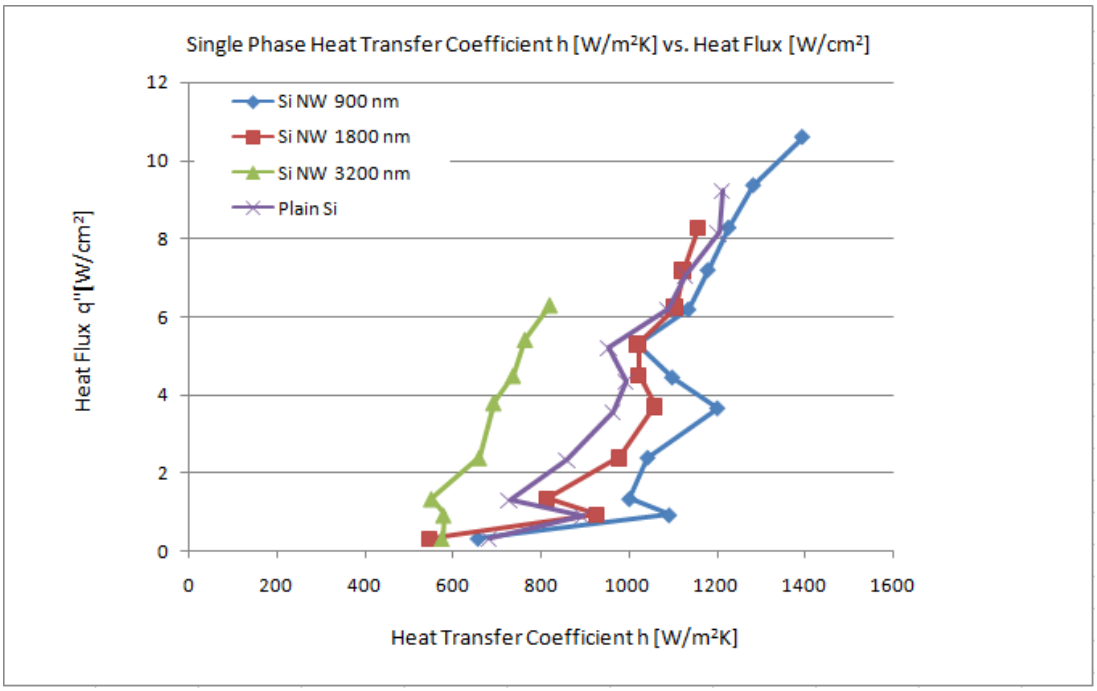

Figure 3.20. Single-phase region heat transfer coefficients vs. various constant heat flux values for all test samples.

The views of SEM images of nanostructured nano plates are shown in Figure 3.21. The images confirmed that the nanostructures are still solid and stable after the experiments. Fracture or failure is not observed. There is no common structural changes instead of nanorods are slightly rounded at the tops. Carbon nanorods have a fracture problem after usage unlike silicone nanorods, which makes silicone as the best choice between them.

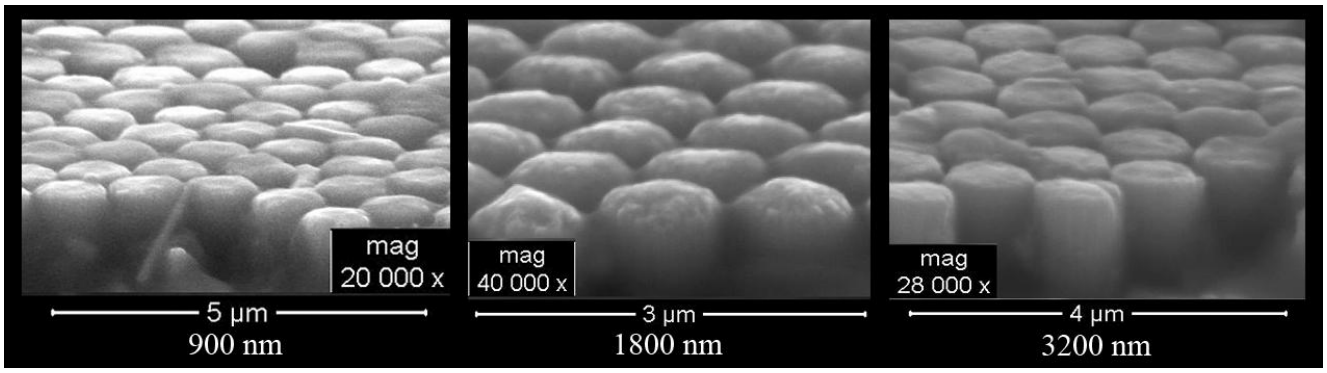

Figure 3.21. The SEM image views of nanorods.

4 CONCLUSION

4.1 Conclusions of Micro Pin Fin Heat Sink Study

In this study, an experimentally tested device was first modeled. The results of the simulated device model were compared to the experimental data related to the corresponding micro pin fin device in the literature to prove the credibility of numerical models. Thereafter, micro pin fin configurations with micro pin-fins of different shapes were modeled, and their thermal-hydraulic performances were compared based on average heat transfer coefficient, h, Nusselt number, Nu, friction factor, f, pressure drop, ΔP, and thermal performance index, η, in the light of streamlines around the modeled micro pin fins. According to the simulations with the circular, cone, hydrofoil, rectangular, square, and triangular shapes, the following conclusions are drawn:

- The highest h is provided by the rectangular shape, which has larger heat transfer area and also promotes flow separation with multiple sharp points on the geometry. The hydrofoil shaped micro pin fin configuration is its closest follower. The result agrees with the previous study of Koşar and Peles [17], who observed that micro pin fins having sharp pointed regions have higher heat transfer coefficients than streamlined pin fins.
- The Nusselt number increases with increasing Reynolds number as observed in the previous studies of Koşar and Peles [17] and Liu et al. [33], and the rectangular shaped pin fin has the highest Nu values.
- The pressure drop, ΔP, increases with the increasing mass flow rate, and the rectangular pin fin has the highest pressure drop among all the pin fin geometries.
- The friction factor of the rectangular shaped pin fin has the highest value among all the pin fin geometries and decreases with increasing Re. Both form drag and friction drag have significant effects on the friction factor over the simulated Re range.
- Thermal performance index (TPI), η, based on the circular micro pin fin increases with the increasing Re, and the cone shaped pin fin has the highest TPI among all the pin fin geometries, which shows cone shaped pin fin could be the most applicable selection for micro pin fin heat sinks.

4.2 Conclusions of Jet Impingement Study

The results gathered from our experimental work indicate the advantageous effects of a vertical nanostructured plate on single and two phase heat transfer enhancement via a jet impingement cooling device. The vertical nanorods integrated to the copper thin film layer on silicon wafer act as nanoscale pin-fins and introduce enhanced surface area. The nanorods also contribute to heat transfer with secondary flows, changing boundary layers developing from the surface and their single crystal property. A single phase average heat transfer enhancement of 22.4% and a two phase average heat transfer enhancement of 85.3% has been realized using the nanostructured plate with vertical nanorods compared to the at plate. The tilted nanorods, on the other hand, failed to contribute to heat transfer and even performed worse than the Cu thin film at plate. This was attributed to the decreased water supply to the base of the plate due to the dense structure of the tilted nanorods and their orientation. Moreover, the configuration of the tilted rods prevents bubble departure and trapped bubbles increase thermal resistance, which, in turn, decreases nucleate boiling heat transfer. As a result, by using a compact setup with integrated vertical nanostructures, the cooling system acts more efficiently compared to its plain surface counterparts, while the orientation of nanostructures is found to be an important parameter for heat transfer.

In the light of the tabulated results, more in-depth systematic studies to control the length, spacing, orientation and diameter of nanorods are critically important for fundamental understanding of heat transfer occurring from the nanostructured surfaces as well as to clarify the potential benefits/limitations of this technology in various applications such as cooling of small micro-electro-mechanical devices used in micro reactors, micro propulsion, biotechnology, fuel cells and air conditioning. Moreover, there is a need to develop empirical correlations for calculating the heat transfer coefficients of the nanostructured surfaces, which can be useful in designing such devices for cooling applications.

4.3 Conclusions of Pool Boiling Study

This study proves positive effects of utilizing nanostructured plates in pool boiler cooling applications. A significant enhancement in heat transfer coefficients at both single-phase (up to its 114%) and boiling regions (up to its 354%) is achieved using nanostructured plates with Si nanowires. Due to the increasing active nucleation site density, surface wettability and heat transfer area, nanostructured surfaces escalate the performance of the cooling system. Furthermore, they are assumed to increase the bubble generation frequency by decreasing the liquid-surface contact angle. It is observed that as the length of the nanowires increases, the enhancement in heat removal performance of the system decreases due to the decreased wettability of the surface.

Since there is an ongoing debate whether the decreasing contact angle would make a positive contribution to boiling heat transfer for a decrease in contact angle would also decrease the bubble diameter [56] authors feel the need to extend the research by providing an accurate measurement of the contact angles of the nanostructured plates used in this study. Moreover, SEM images of the plates after being experimented on will be obtained in order to determine the durability of the nanostructures under the changing operational conditions. A mathematical correlation of heat transfer characteristics of the system needs to be obtained since no existing correlation in literature completely coincides with the findings in this research.

Under the light of the presented data, it is safe to say that nanostructured plates featuring Si nanowires make a significant contribution to the heat removal performance of the pool boiling system and the enhancement in heat transfer coefficients in both single-phase and boiling regions is very promising.

4.4 Contribution of This Study to the Literature

Micro pin fin heat sinks have been a popular research topic for last few decades and are more and more popular due to the significance of heat removal in increasing heat transfer performances of components or systems. In addition to the conventional pin fin shapes, different pin fin geometries are evaluated in this study. According to the results obtained from micro pin fin heat sink study, cone shaped pin fin has the best thermal performance index, which makes it the best applicable option amongst seven different shapes that the study covered. It could be deduced that the use of pin fins with

non-conventional shape could be attractive particularly at relatively under certain working conditions.

In our jet impingement study, our main goal is to contribute to literature by investigating the effect of changing nanorod orientation on heat removal performance of heat sinks. According to the results gathered from our experimental study, the nanostructured plate with tilted nanorods have shown the worst cooling performance compared to the plain surfaced control sample and the nanostructured plate with vertical nanorods. In this study, pioneering efforts were made in order to eliminate the lack of knowledge in literature concerning the effect of changing nanorod orientation and further studies leading to optimization of parameters such as tilt angle, nanorod spacing and length, which would possibly result in an ideal tilted nanorod configuration capable of increasing heat removal rate even better than the vertical nanorods, were encouraged.

A compact pool boiler heat sink utilizing nanostructured surfaces is designed to investigate the effect of changing nanowire length on heat removal performance of the system. It is observed that as the length of the nanowires increases, the enhancement in heat removal performance of the system decreases due to the decreased wettability of the surface and increased thermal resistance. This study has shown that short nanowires have the best heat removal performance among the samples used in our experiments. This study will motivate researchers to attempt to determine the optimum length of the nanowires integarated to the surfaces of microsystems to obtain the best heat removal performance in the future.

REFERENCES

1] D. B. Tuckerman and R. F. W. Pease, "High-Performance Heat Sinking for VLSI," *IEEE Electron Device Letters,* vol. 2, pp. 126-129, 1981.

2] R. J. Philips, "Micro-Channel Heat Sinks," *Advances in Thermal Modeling of Thermal Electronic Components,* vol. 2, pp. 109-184, 1990.

3] [Online]. Available: http://www.build-your-own-computer.net/cpu-cooling.html. [Accessed 23 July 2012].

4] R. W. Knight, D. J. Hall, J. S. Goodling and R. C. Jaeger, "Heat Sink Optimization with Application to Microchannels," *IEEE Transactions on Components, Hybrids and Manufacturing Technology,* vol. 15, pp. 832-842, 1992.

5] T. M. Harms, M. J. Kazmierczak and F. M. Cerner, "Developing Convective Heat Transfer in Deep Rectangular Microchannels," *International Journal of Heat and Fluid Flow,* vol. 20, pp. 149-157, 1999.

6] A. G. Fedorov and R. Viskanta, "Three-Dimensional Conjugate Heat Transfer in the Microchannel Heat Sink for Electronic Packaging," *International Journal of Heat and Mass Transfer,* vol. 43, pp. 399-415, 2000.

7] W. Qu and I. Mudawar, "Analysis of Three-Dimensional Heat Transfer in Micro-Channel Heat Sinks," *Journal of Heat and Mass Transfer,* vol. 45, pp. 3973-3985, 2002.

8] W. Qu and I. Mudawar, "Experimental and Numerical Study of Pressure Drop and Heat Transfer in a Single-Phase Micro-Channel Heat Sink," *International Journal of Heat and Mass Transfer,* vol. 45, pp. 2549-2565, 2002.

9] J. Li, G. P. Peterson and P. Cheng, "Three-Dimensional Analysis of Heat Transfer in a Micro-Heat Sink with Single Phase Flow," *International Journal of Heat and Mass Transfer,* vol. 47, pp. 4215-4231, 2004.

10] P. S. Lee, S. V. Garimella and D. Liu, "Investigation of Heat Transfer in Rectangular Microchannels," *International Journal of Heat and Mass Transfer,* vol. 48, pp. 1688-1704, 2005.

11] M. Wong, I. Owen, C. J. Sutcliffe and A. Puri, "Convective Heat Transfer and Pressure Loses Across Novel Heat Sinks Fabricated by Selective Laser Melting," *International Journal of Heat and Mass Transfer,* vol. 52, pp. 281-288, 2009.

12] B. A. Jasperson, Y. Jeon, K. T. Turner, F. E. Pfefferkorn and W. Qu, "Comparison of Micro-Pin-Fin and Microchannel Heat Sinks Considering Thermal-Hydraulic Performance and Manufacturability," *IEEE Transactions on Components, Packaging and Manufacturing Technology,* vol. 33, pp. 148-160, 2010.

13] Y. Peles, A. Koşar, C. Mishra, C. -J. Kuo and B. Schneider, "Forced Convective Heat Transfer Across a Pin Fin Micro Heat Sink," *International Journal of Heat and Mass Transfer,* vol. 48, pp. 3615-3627, 2005.

14] A. Koşar, C. Mishra and Y. Peles, "Laminar Flow across a Bank of Low Aspect Ratio Micro Pin-fins," *ASME Journal of Fluids Engineering,* vol. 127, pp. 419-430, 2005.

15] A. Koşar and Y. Peles, "Thermal-Hydraulic Performance of MEMSBased Pin Fin Heat Sink," *ASME Journal of Heat Transfer,* vol. 128, pp. 121-131, 2006.

16] A. Koşar and Y. Peles, "Convective flow of refrigerant (R-123) across a bank of micro pin-fins," *International Journal of Heat and Mass Transfer,* vol. 49, pp. 3142-3155, 2006.

17] A. Koşar and Y. Peles, "Micro Scale Pin-fin Heat Sinks-Parametric Performance Evaluation Study," *IEEE Transactions on Components, Packaging and Manufacturing Technology,* vol. 30, pp. 855-865, 2007.

R. S. Prasher, J. Dirner, J. Y. Chang, A. Myers, D. Chau, D. He and S. Prstic, "Nusselt
18] Number and Friction Factor of Staggered Arrays of Low Aspect Ratio Micro-Pin-Fins Under Cross Flow for Water As Fluid," *ASME Journal of Heat Transfer,* vol. 129, pp. 141-153, 2007.

T. J. John, B. Mathew and H. Hegab, "Parametric Study on the Combined Thermal and
19] Hydraulic Performance of Single Phase Micro Pin-Fin Heat Sinks part I: Square and Circle Geometries," *International Journal of Thermal Science ,* vol. 49, pp. 2177-2190, 2010.

J. F. Tullius, T. K. Tullius and Y. Bayazitoglu, "Optimization of Microstructured Fins in
20] Minichannels," in *Proceedings of TMNN-2011/068*, 2011.

J. F. Tullius, T. K. Tullius and Y. Bayazitoglu, "Optimization of Short Micro Pin Fins in
21] Minichannels," *International Journal of Heat and Mass Transfer,* in press.

M. K. Chyu and Y. C. Hsing, "Convective Heat Transfer of Cubic Fin Arrays in a Narrow
22] Channel," *ASME Journal of Turbomachining,* vol. 120, pp. 362-367, 1998.

A. Koşar, C. Kuo and Y. Peles, "Hydofoil-Based Micro Pin Fin Heat Sink," in
23] *IMECE2006-13257*, 2006.

B. E. Short, P. E. Raad and D. C. Price, "Performance of Pin Fin Cast Aluminum
24] Coldwalls, Part 1: Friction Factor Correlation," *Journal of Thermophysics and Heat Transfer,* vol. 16, pp. 389-396, 2002.

B. E. Short, P. E. Raad and D. C. Price, "Performance of Pin Fin Cast Aluminum
25] Coldwalls, Part 2: Colburn j-Factor Correlations," *Journal of Thermophysics and Heat Transfer,* vol. 16, pp. 397-403, 2002.

K. A. Moores and Y. K. Joshi, "Effect of Tip Clearance on the Thermal and
26] Hydrodynamic Performance of a Shrouded Pin Fin Array," *ASME Journal of Heat Transfer,* vol. 125, pp. 999-1006, 2003.

A. Siu-Ho, W. Qu and F. Pfefferkorn, "Experimental Study of Pressure Drop and Heat
27] Transfer in a Single-Phase Micro-Pin-Fin Heat Sink," *ASME Journal of Electronic Packaging,* vol. 129, pp. 479-487, 2007.

W. Qu and A. Siu-Ho, "Liquid Single-Phase Flow in an Array of Micro-Pin-Fins – Part I:
28] Heat Transfer Characteristics," *ASME Journal of Heat Transfer,* vol. 130, pp. 122402-1 - 122402-11, 2008.

W. Qu and A. Siu-Ho, "Liquid Single-Phase Flow in an Array of Micro-Pin-Fins – Part II:
29] Pressure Drop Characteristics," *ASME Journal of Heat Transfer,* vol. 130, pp. 122405-1 – 122405-4, 2008.

T. -M. Jeng and S. -C. Tzeng, "Pressure Drop and Heat Transfer of Square Pin-fin
30] Arrays in In-line and Staggered Arrangements," *International Journal of Heat and Mass Transfer,* vol. 50, pp. 2364-2375, 2006.

W. A. Khan, J. R. Culham and M. M. Yovanovich, "The Role of Fin Geometry in Heat
31] Sink Performance," *Journal of Electronic Packaging,* vol. 128, pp. 324-330, 2006.

A. Koşar, M. R. Özdemir and M. Keskinöz, "Pressure Drop across Micro-pin Fin Heat
32] Sinks under Unstable Boiling Conditions," *International Journal of Thermal Science ,* vol. 49, pp. 1253-1263, 2010.

M. Liu, D. Liu, S. Xu and Y. Chen, "Experimental Study on Liquid Flow and Heat
33] Transfer in Micro Square Pin Fin Heat Sink," *International Journal of Heat and Mass Transfer,* vol. 54, pp. 5602-5611, 2011.

M. Koz, M. R. Özdemir and A. Koşar, "Parametric Study on the Effect of End walls on
34] Heat Transfer and Fluid Flow across a Micro Pin-fin," *International Journal of Thermal Science,* vol. 50, pp. 1073-1084, 2011.

B. Agostini, M. Fabbri, J. E. Park, L. Wojtan, J. R. Thome and B. Michel, "State of the

35] Art of High Heat Flux Cooling Technologies," *Heat Transfer Engineering,* vol. 28, no. 4, pp. 258-281, 2007.

36] T. S. O'Donovan and D. B. Murray, "Jet Impingement Heat Transfer - Part 1: Analysis of Heat Transfer and Local Velocity Distributions," *International Journal of Heat and Mass Transfer,* vol. 50, pp. 3291-3301, 2007.

37] R. Cardenas, P. Mani and V. Narayanan, "Saturated Mini Jet Impingement Boiling," in *Proceedings of ASME 2010 8th International Conference on Nanochannels, Microchannels, and Minichannels, ICNMM2010-30749*, Montreal, Canada, 2010.

38] D. Babic, D. B. Murray and A. A. Torrance, "Mist Jet Cooling of Grinding Processes," *Int. J. Mach. Tools Manufact.,* vol. 45, pp. 1171-1177, 2005.

39] A. Royne and C. Dey, "Experimental Study of a Jet Impingement Device for Cooling of Photovoltaic Cells Under High Concentration," in *Proceedings of Solar 2004: Life, the Universe and Renewables*, 2004.

40] L. -H. Chien and C. -Y. Chang, "An experimental study of two-phase multiple jet cooling on finned surfaces using a dielectric fluid," *Applied Thermal Engineering ,* vol. 31, no. 11-12, pp. 1983-1993, 2011.

41] M. Sesen, W. Khudhayer, T. Karabacak and A. Kosar, "A Compact Nanostructure Integrated Pool Boiler for Microscale Cooling Applications," *Micro&Nano Letters,* vol. 5, no. 4, pp. 203-206, 2010.

42] M. Sesen, W. Khudhayer, T. Karabacak, A. B. Kosar, B. A. Ahishalioglu and A. Kosar, "A Compact Nanostructure Enhanced Heat Sink with Flow in a Rectangular Channel," in *Proceedings of the ASME 2010 10th Biennial Conference on Engineering Systems Design & Analysis, ESDA2010-25336*, Istanbul, Turkey, 2010.

43] H. S. Ahn, V. Sathyamurthi and B. D., "Pool Boiling Experiments on a Nano-Structured Surface," *IEEE Transactions on Components and Packaging Technologies,* vol. 32, no. 1, pp. 156-165, 2009.

44] M. Zhang and K. Lian, "Using bulk micromachined structures to enhance pool boiling heat transfer," *Microsystem Technologies,* vol. 14, no. 9-11, pp. 1499-1505, 2007.

45] K. Kordás, G. Tóth, P. Moilanen, K. M., J. Vähäkangas, A. Uusimäki, R. Vajtaia and A. P. M., "Chip Cooling with Integrated Carbon Nanotube Microfin Architectures," *Applied Physics Letters,* vol. 90, no. 12, pp. 123105/1-123105/3., 2007.

46] W. I. Son, J.-H. Hong and J.-M. Hong, "Fabrication of Micro-Heatsink by Nanotemplate Synthesis and its Cooling Characteristics," *Span. Conf. Electron Devices,* Vols. 2-4, pp. 439-442, 2005.

47] B. Weigand and S. Spring, "Multiple Jet Impingement – A Review," *Int. Symp on Heat Transfer in Gas Turbine Systems,* 2009.

48] D. J. Womac, G. Aharoni, S. Ramadhyani and F. P. Incropera, ""Single Phase Liquid Jet Impingement Cooling of Small Heat Sources,"," *Proceedings of the International Heat Transfer Conference,* pp. 149-154, 1990.

49] S. V. Garimella and R. A. Rice, "Confined and Submerged Liquid Jet Impingement Heat Transfer," *Journal of Heat Transfer,* vol. 117, pp. 871-877, 1995.

50] S. V. Garimella and B. Nenaydykh, "Nozzle-Geometry Effects in Liquid Jet Impingement Heat Transfer," *International Journal of Heat and Mass Transfer,* vol. 39, no. 14, pp. 2915-2923, 1996.

51] K. Robbie, G. Beydaghyan, T. Brown, C. Dean, J. Adams and C. Buzea, "Ultrahigh Vacuum Glancing Angle Deposition System for Thin Films with Controlled Three-Dimensional Nanoscale Structure," *Rev. Sci. Instrum.,* vol. 75, no. 4, pp. 1089-1097, 2004.

T. Karabacak and T.-M. Lu, in *Handbook of Theoretical and Computational*

52] *Nanotechnology*, M. Rieth and W. Schommers, Eds., Stevenson Ranch, CA, American Scientific Publishers, 2005, p. 729.

53] T. Karabacak, G. C. Wang and T.-M. Lu, "Physical Self-Assembly and the Nucleation of 3D Nanostructures by Oblique Angle Deposition," *J. Vac. Sci. Technol. A,* vol. 22, no. 4, pp. 1778-1784, 2004.

54] C. Li, Z. Wang, P.-I. Wang, Y. Peles, N. Koratkar and G. P. Peterson, "Nanostructured Copper Interfaces for Enhanced Boiling," *Small,* vol. 4, no. 8, p. 1084–1088, 2008.

55] I. Mudawar, "Assesment of High-Heat-Flux Thermal Management Schemes," *IEEE Transactions on Components and Packaging Technologies,* vol. 24, no. 2, pp. 122-140, 2001.

56] Hendricks, J. Terry , S. Krishnan, C. Choi, C. H. Chang and B. Paul, "Enhancement of Pool-Boiling Heat Transfer Using Nanostructured Surfaces on Aluminum and Copper," *International Journal of Heat and Mass Transfer,* vol. 53, pp. 3357-3365, 2010.

57] K. J. Park and D. Jung, "Enhancement of Nucleate Boiling Heat Transfer Using Carbon Nanotubes," *International Journal of Heat and Mass Transfer,* vol. 50, pp. 4499-4502, 2007.

58] P. Xiao, W. J. Li and R. Du, "Microbubble Generation Using Carbon Nanotubes Heating Elements," *IEEE Transactions on Nanotechnology,* vol. 10, no. 3, pp. 520-527, 2011.

59] S. Ujereh, T. S. Fisher, I. Mudawar, P. B. Amama and W. Qu, "Enhanced Pool Boiling using Carbon Nanotube Arrays on a Silicon Surface," in *ASME Int. Mechanical Engineering Congress & Exposition*, Orlando, FL, 2005.

60] P. Keblinski, J. A. Eastman and D. G. Cahill, "Nanofluids for Thermal Transport," *Mater. Today,* vol. 8, no. 6, pp. 36-44, 2005.

61] I. C. Bang and S. H. Chang, "Boiling Heat Transfer Performance and Phenomena of Al2O3–Water Nano-Fluids from a Plain Surface in a Pool," *Int. J. Heat Mass Transfer,* vol. 48, no. 12, p. 2407–2419, 2005.

62] S. Vemuri and K. J. Kim, "Pool Boiling of Saturated FC-72 on Nano-Porous Surface," *Int. Commun. Heat Mass Transf.,* vol. 32, no. 1-2, p. 27–31, 2005.

63] D. Milanova and R. Kumar, "Role of Ions in Pool Boiling Heat Transfer of Pure and Silica Nanofluids," *Appl. Phys. Lett.,* vol. 87, no. 23, 2005.

64] S. M. You, J. H. Kim and K. H. Kim, "Effect of Nanoparticles on Critical Heat Flux of Water in Pool Boiling Heat Transfer," *Appl. Phys. Lett.,* vol. 83, no. 16, 2003.

65] H. Kim, J. Kim and M. Kim, "Effect of Nanoparticles on CHF Enhancement in Pool Boiling of Nano-Fluids," *International Journal of Heat and Mass Transfer,* vol. 49, no. 25-26, pp. 5070-5074, 2006.

66] S. J. Kim, I. C. Bang, J. Buongiorno and L. W. Hu, "Surface Wettability Change during Pool Boiling of Nanofluids and Its Effect on Critical Heat Flux," *Int. J. Heat Mass Transfer,* vol. 50, no. 19-20, p. 4105–4116, 2007.

67] H. Honda, H. Takamatsu and J. J. Wei, "Enhanced Boiling of FC-72 on Silicon Chips with Micro-Pin-Fins and Submicron-Scale Roughness," *J. Heat Transfer,* vol. 124, no. 2, p. 383–390, 2002.

68] M. Sesen, W. J. Khudhayer, T. Karabacak and A. Kosar, "A Compact Nanostructure Integrated Pool Boiler for Microscale Cooling Applications," in *ASME Int. Mechanical Engineering Congress & Exposition, IMECE2009–11008*, Orlando, FL, 2009.

69] P. Vassallo, R. Kumar and S. D'Amico, "Pool Boiling Heat Transfer Experiments in Silica–Water Nano-Fluids," *Int. J. Heat Mass Transfer,* vol. 47, no. 2, p. 407–411, 2004.

J. A. Eastman, S. U. S. Choi, S. Li, W. Yu and L. J. Thompson, "Anomalously Increased

70] Effective Thermal Conductivities of Ethylene Glycol-Based Nanofluids Containing Copper Nanoparticles," *Applied Physics Letters,* vol. 78, no. 6, pp. 718-720, 2001.

71] H. Kim, J. Kim and M. Kim, "Experimental Study on CHF Characteristics of Water TiO2 Nano-Fluids," *Nucl. Eng. Technol.,* vol. 38, no. 1, p. 61–68, 2006.

72] H. A. Van Der Vorst, "A Fast and Smoothly Converging Variant of Bi-CG for the Solution of Nonsymmetric Linear Systems," *SIAM Journal on Scientific and Statistical Computing,* vol. 13, pp. 631-644, 1992.

73] A. Greenbaum, "Iterative Methods for Linear Systems, Frontiers in Applied Mathematics," *SIAM,* vol. 17, 1997.

74] F. P. Incropera, D. P. DeWitt, T. L. Bergman and A. S. Lavine, in *Fundamentals of Heat and Mass Transfer*, 6th ed., New York, Wiley, 2007, p. 531.

75] L. Dong, R. Dong-Ho, K. Kyung, C. Hyung and M. Hee-Koo, "Heat Transfer and Flow Temperature Measurements in a Rotating Triangular Channel with Various Rib Arrangements," *Heat and Mass Transfer,* vol. 45, pp. 1543-1553, 2009.

76] T. Karabacak, J. S. DeLuca, D. Ye, P.-I. Wang, W. G.-C. and L. T.-M., "Low Temperature Melting of Copper Nanorod Arrays," *J. Appl. Phys.,* vol. 99, no. 6, 2006.

77] T. Karabacak, P.-I. Wang, G.-C. Wang and T.-M. Lu, "Phase Transformation of Single Crystal β-Tungsten Nanorods at Elevated Temperatures," *Thin Solid Films,* vol. 493, no. 1-2, pp. 293-296, 2005.

78] T. Karabacak, P.-I. Wang, G.-C. Wang and T.-M. Lu, "Growth of Single Crystal Tungsten Nanorods by Oblique Angle Sputter Deposition," *Mat. Res. Soc. Symp. Proc.,* vol. 788, p. 75, 2004.

79] W. J. Khudhayer, A. U. Shaikh and T. Karabacak, "Platinum Nanorod Arrays with Preferred Morphological and Crystal Properties for Oxygen Reduction Reaction," *Advanced Science Letters,* vol. 4, pp. 1-9, 2011.

80] H. Martin, "Heat and Mass Transfer Between Impinging Gas Jets and Solid Surfaces," *Advances in Heat Transfer,* vol. 13, pp. 1-60, 1977.

81] S. J. Kline and F. A. McClintock, "Describing Uncertainties in Single-Sample Experiments," in *Mech. Eng. p.3*, 1953.

82] B. G. Prevo and O. D. Velev, "Controlled, Rapid Deposition of Structured Coatings from Micro- and Nanoparticle Suspensions," *Langmuir,* vol. 20, no. 6, pp. 2099-2107, 2004.

83] A. S. Alagoz and T. Karabacak, in *MRS Proceedings*, in press.

84] B. R. Munson, D. F. Young and T. H. Okiishi, in *Fundamentals of Fluid Mechanics*, 3rd ed., New York, Wiley, 1998, pp. 591-610.

85] F. White , in *Fluid Mechanics*, 4th ed., New York, McGrawHill, 1999, pp. 456-461.

86] K. Bilen, U. Akyol and S. Yapici, "Heat Transfer and Friction Correlations and Thermal Performance Analysis for a Finned Surface," *Energy Conversion and Management,* vol. 42, pp. 1071-1083, 2001.

87] W. J. Khudhayer, R. Sharma and T. Karabacak, "Hydrophobic Metallic Nanorods with Teflon Nanopatches," *Nanotechnology,* vol. 20, no. 27, 2009.

88] F. P. Incropera and D. P. Dewitt, Fundamentals of Heat and Mass Transfer, 6th ed., Wiley, 2006.

89] J. P. McHale and S. V. Garimella, "Bubble Nucleation Characteristics in Pool Boiling of a Wetting Liquid on Smooth and Rough Surfaces," *International Journal of Multiphase*

Flow, vol. 36, pp. 249-260, 2010.